Article

Somatic mutation landscapes at single-molecule resolution

https://doi.org/10.1038/s41586-021-03477-4

Received: 13 November 2020

Accepted: 22 March 2021

Published online: 28 April 2021

Check for updates

Federico Abascal[1], Luke M. R. Harvey[1,11], Emily Mitchell[1,2,11], Andrew R. J. Lawson[1,11], Stefanie V. Lensing[1,11], Peter Ellis[1,9,11], Andrew J. C. Russell[1], Raul E. Alcantara[1], Adrian Baez-Ortega[1], Yichen Wang[1], Eugene Jing Kwa[1], Henry Lee-Six[1], Alex Cagan[1], Tim H. H. Coorens[1], Michael Spencer Chapman[1], Sigurgeir Olafsson[1], Steven Leonard[1], David Jones[1], Heather E. Machado[1], Megan Davies[2], Nina F. Øbro[2,3], Krishnaa T. Mahubani[3,4,5], Kieren Allinson[6], Moritz Gerstung[7], Kourosh Saeb-Parsy[4,5], David G. Kent[2,8], Elisa Laurenti[2,3], Michael R. Stratton[1], Raheleh Rahbari[1], Peter J. Campbell[1,3], Robert J. Osborne[1,10] ✉ & Iñigo Martincorena[1] ✉

Somatic mutations drive the development of cancer and may contribute to ageing and other diseases[1,2]. Despite their importance, the difficulty of detecting mutations that are only present in single cells or small clones has limited our knowledge of somatic mutagenesis to a minority of tissues. Here, to overcome these limitations, we developed nanorate sequencing (NanoSeq), a duplex sequencing protocol with error rates of less than five errors per billion base pairs in single DNA molecules from cell populations. This rate is two orders of magnitude lower than typical somatic mutation loads, enabling the study of somatic mutations in any tissue independently of clonality. We used this single-molecule sensitivity to study somatic mutations in non-dividing cells across several tissues, comparing stem cells to differentiated cells and studying mutagenesis in the absence of cell division. Differentiated cells in blood and colon displayed remarkably similar mutation loads and signatures to their corresponding stem cells, despite mature blood cells having undergone considerably more divisions. We then characterized the mutational landscape of post-mitotic neurons and polyclonal smooth muscle, confirming that neurons accumulate somatic mutations at a constant rate throughout life without cell division, with similar rates to mitotically active tissues. Together, our results suggest that mutational processes that are independent of cell division are important contributors to somatic mutagenesis. We anticipate that the ability to reliably detect mutations in single DNA molecules could transform our understanding of somatic mutagenesis and enable non-invasive studies on large-scale cohorts.

Somatic mutations occur in our cells as we age. Because most somatic mutations are only present in small groups of cells or even in single cells, studying somatic mutagenesis has been challenging and has required special approaches. This includes ultra-deep sequencing of small biopsies[3–5], laser microdissection[6–8], isolation of single cells followed by in vitro expansion into organoids or colonies[9–11] and single-cell sequencing[12–14]. Although these technologies are changing our understanding of somatic mutagenesis, the error rates of single-cell approaches have—until recently[15]—been too high[16] and other approaches are limited to mitotically active cell types.

As a result of these technical limitations, the rates and patterns of somatic mutation across most human cell types remain underexplored. This is especially the case for non-dividing cells, including terminally differentiated cells in mitotically active tissues, which are often responsible for tissue function, and cells in post-mitotic tissues, such as cortical neurons or cardiac muscle, which are of particular interest in human ageing, neurodegeneration and cardiovascular disease. Post-mitotic tissues can also inform on the contribution of cell division and DNA replication to somatic mutation in human tissues. To address these questions, we developed a sequencing protocol that enables the study of somatic mutations in any tissue or cell population by reliably detecting somatic mutations in single DNA molecules.

Nanorate sequencing

Several protocols have been developed to increase the accuracy of standard sequencing by barcoding individual molecules of DNA and sequencing each molecule multiple times, reducing error rates by

[1]Wellcome Sanger Institute, Hinxton, UK. [2]Wellcome–MRC Cambridge Stem Cell Institute, Cambridge Biomedical Campus, Cambridge, UK. [3]Department of Haematology, University of Cambridge, Cambridge, UK. [4]Department of Surgery, University of Cambridge, Cambridge, UK. [5]NIHR Cambridge Biomedical Research Centre, Cambridge Biomedical Campus, Cambridge, UK. [6]Cambridge Brain Bank, Division of the Human Research Tissue Bank, Addenbrooke's Hospital, Cambridge, UK. [7]European Molecular Biology Laboratory, European Bioinformatics Institute (EMBL-EBI), Hinxton, UK. [8]York Biomedical Research Institute, Department of Biology, University of York, York, UK. [9]Present address: Inivata, Babraham Research Campus, Cambridge, UK. [10]Present address: Biofidelity, Cambridge Science Park, Cambridge, UK. [11]These authors contributed equally: Luke M. R. Harvey, Emily Mitchell, Andrew R. J. Lawson, Stefanie V. Lensing, Peter Ellis. ✉e-mail: r.osborne@biofidelity.com; im3@sanger.ac.uk

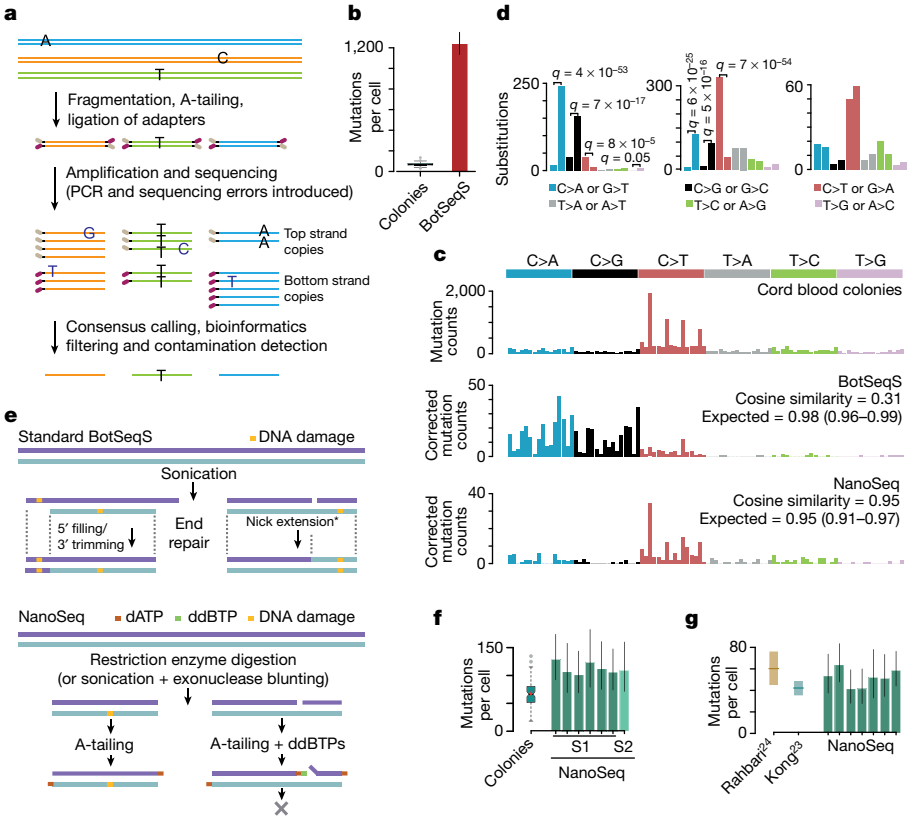

Fig. 1 | BotSeqS and NanoSeq sequencing protocols. a, Duplex sequencing protocol. **b**, BotSeqS mutation burden estimates in cord blood granulocytes compared to 100 single-cell-derived blood colonies from two donors. **c**, BotSeqS and NanoSeq substitution profiles for cord blood granulocytes, and cosine similarities (Methods) with the cord blood colonies profile. The 95% confidence intervals are included in parentheses. **d**, Substitution imbalances are present in standard BotSeqS protocols but absent from NanoSeq data (Extended Data Figs. 1, 2 show further details for a library of granulocytes from a 59-year-old donor). Left, BotSeqS data from this study; middle, BotSeqS data from a previous study[20]; right, NanoSeq data. Imbalances were tested with a binomial test and *P* values were corrected with Benjamini and Hochberg's false-discovery rate method. **e**, Standard BotSeqS (top) and NanoSeq (bottom) protocols for library preparation. Displacement activity of the DNA polymerase is indicated by an asterisk. **f**, **g**, NanoSeq mutation burden estimates for cord blood granulocytes (**f**; S1/PD48442, $n = 6$ libraries; S2/PD47269, $n = 1$) and sperm from a 21-year-old donor ($n = 7$) (**g**) compared to blood colonies and estimates from parent–child trios, respectively. **b**, **f**, **g**, Bars show point estimates and their 95% Poisson confidence intervals. **b**, **f**, Box plot shows the interquartile range, median, 95% confidence interval for the median, and outliers as grey dots. **f**, The mean and its 95% confidence interval are shown in red.

single-molecule consensus[17]. The most accurate approaches use duplex consensus sequencing[18,19], sequencing copies of both strands of a DNA molecule to remove sequencing errors (present in individual reads) and PCR errors (present in copies of one of the two strands) (Fig. 1a). Duplex sequencing has a theoretical error rate of less than 10^{-9} errors per base pair (bp), the probability of two early and complementary PCR errors in both strands[17]. Given that this rate is lower than the typical mutational load of human tissues, it raises the possibility of quantifying somatic mutation rates in genetically heterogeneous samples, by detecting somatic mutations in single DNA molecules. This is the rationale of BotSeqS, a whole-genome duplex sequencing protocol[20] (Fig. 1a). In practice, however, mapping errors and some library preparation artefacts can violate the assumed independence of both strands[20,21]. The actual error rates of duplex sequencing protocols have remained difficult to measure owing to the lack of control samples with low and known mutation rates[17].

To evaluate the performance of BotSeqS, we used samples of cord blood, comparing BotSeqS of bulk granulocytes from a neonate to standard sequencing of 100 single-cell-derived colonies from two neonates as a control. On average, single-cell-derived colonies had 66 mutations per cell, which were dominated by C>T mutations at CpG sites. By contrast, BotSeqS estimated 1,240 mutations per diploid genome, which were dominated by C>A and C>G mutations (Fig. 1b, c). Analysing the distribution of substitutions across BotSeqS reads revealed a large excess of G>T/C and C>T substitutions near the 5′ ends of DNA fragments, and an imbalance over the complementary C>A/G and G>A substitutions that affected the entire read length (Fig. 1d and Extended Data Figs. 1, 2). These imbalances are incompatible with real mutations and reflect errors introduced during library preparation[22] (Methods and Supplementary Note 1). We found the same imbalances, with a much larger C>T component, in the original BotSeqS publication[20] (Fig. 1d). Extensive trimming of read ends only partially alleviated these errors (Extended Data Fig. 2). Overall, we estimate that BotSeqS introduced approximately 1,200 errors per diploid genome in our samples (equivalent to around 2×10^{-7} errors per bp).

On the basis of the error patterns, we reasoned that end repair was probably responsible for most of the errors, by converting DNA damage in single strands of DNA into double-stranded errors (Fig. 1e and Extended Data Fig. 1c, d). To solve this, we developed NanoSeq, a protocol that prevents copying errors between strands by avoiding end repair and by blocking nick extension. First, we replaced sonication and end repair with restriction enzyme fragmentation (Fig. 1e, Methods, Supplementary Table 3 and Supplementary Note 2). Although restriction enzymes provide partial coverage of the genome (29% using HpyCH4V), the fraction covered is sufficiently random to accurately estimate mutation rates and signatures. They also enable the generation of NanoSeq libraries from as little as 1 ng of DNA (Methods). Alternatively, we show that sonication followed by exonuclease blunting can be used for applications that require whole-genome coverage (Methods, Extended Data Fig. 3 and Supplementary Note 3). Second,

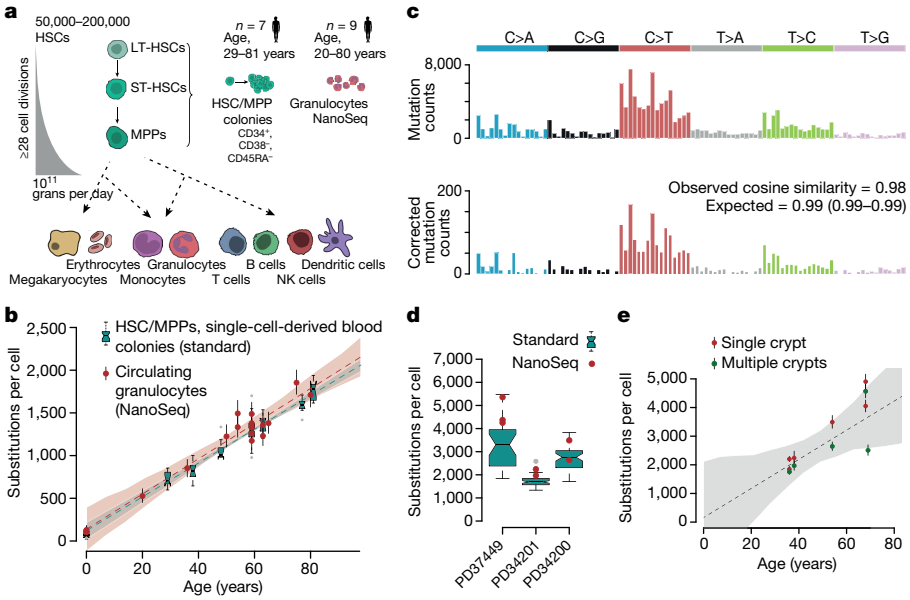

Fig. 2 | Mutation in stem and differentiated cells. a, Schematic representation of the haematopoietic lineage showing which cell types and donors were analysed. Grans, granulocytes; LT-HSCs and ST-HSCs, long-term and short-term HSCs, respectively. **b**, Substitutions per cell for donors of different ages, comparing granulocytes and single-cell-derived blood colonies. NanoSeq estimates for granulocytes (red dots) obtained for one library per donor except for donors of ages 54 ($n = 2$), 63 ($n = 2$) and 59 ($n = 5$). Standard sequencing estimates are shown as box plots and based on 10 colonies per donor, except for the 59-year-old donor ($n = 110$) and cord blood ($n = 100$). **c**, Substitution profiles for granulocytes and blood colonies and their cosine similarity (Methods) for the 59-year-old donor. Top, 110 colonies from a previous study[26]. Bottom, 6 libraries analysed by NanoSeq. **d**, Burden estimates in colonic crypts from three donors, comparing standard methods (box plots) and NanoSeq (red dots; $n = 3$, 2 and 2 libraries per donor). Box plots: PD37449, 36-year-old woman, $n = 29$ crypts; PD34201, 38-year-old man, $n = 56$ crypts; PD34200, 54-year-old man, $n = 49$ crypts. **e**, Accumulation of substitutions throughout life in colonic crypts from five donors, excluding substitutions attributed to the episodic colibactin signature (NanoSeq analysis). **b**, **d**, Dots and lines show point estimates and their corresponding 95% Poisson confidence intervals, respectively. **b**, **d**, Box plots show the interquartile range, median, 95% confidence interval for the median, with outliers as grey dots. **b**, **e**, Linear mixed regression models for granulocytes (red dashed line), blood colonies (dark cyan dashed line) and colonic crypts (black dashed line), with 95% confidence intervals calculated through parametric bootstrapping (Methods). Regression intercepts and slopes are provided in Supplementary Table 8.

we introduced non-A dideoxynucleotides (ddBTPs) during A-tailing, to avoid errors from nick extension (Fig. 1e, Methods, Extended Data Fig. 1e and Supplementary Note 4). Adapters with sufficiently diverse random barcodes were used to create single-molecule-derived read families (Supplementary Note 5).

If duplicate rates are not optimized, duplex sequencing approaches can suffer from low efficiency owing to suboptimal read family sizes[20]. We use mathematical modelling of family sizes and PCR quantification of the library to maximize the duplex coverage independently of the amount of input DNA (Methods and Extended Data Fig. 4a–d). A robust bioinformatics pipeline was also developed to avoid false-positive mutation calls from mapping errors and from low-level DNA contamination (Extended Data Fig. 4e, f, Methods and Supplementary Note 6), and to distinguish germline from somatic mutations.

Applying NanoSeq to cord blood granulocytes yielded an estimated mutation rate of 109 mutations per cell (95% Poisson confidence intervals, 95–125) (Fig. 1f). The small difference with the colonies could be due to NanoSeq errors and/or a higher mutation burden in granulocytes than in cord blood stem cells. Consistent with most of the mutations detected by NanoSeq being genuine, no substitution imbalances were detected in the NanoSeq calls (Fig. 1d) and no significant differences were found between the mutational spectra of colonies and granulocytes (Fig. 1c and Methods). As an additional low-burden control, we applied NanoSeq to a sperm sample from a 21-year-old donor. Seven NanoSeq replicates of the sperm sample yielded low mutation burdens, with around 52 mutations per haploid sperm cell (1.8×10^{-8} mutations per bp or approximately 2.5 mutations per year per cell), consistent with current estimates of the mutation rate in the paternal germline from trio studies[23,24] (Fig. 1g). Together, the sperm and cord blood data indicate that the error rate of NanoSeq is lower than 5×10^{-9} errors per bp (fewer than 30 errors per diploid genome), two orders of magnitude lower than the BotSeqS error rate and the somatic mutation load of most human tissues studied to date. Analysis of insertions and deletions (indels) also revealed an indel error rate of less than 3×10^{-9} errors per bp (Methods, Extended Data Fig. 5c and Supplementary Note 8).

The extremely low error rate of NanoSeq, in the nano range, enables the reliable detection of somatic mutations in single DNA molecules, facilitating the study of somatic mutations in any tissue or cell population. We took advantage of this ability to study non-dividing cells across four tissues, addressing two traditionally difficult questions in the field of somatic mutagenesis: the difference in mutation rates between stem cells and terminally differentiated cells in mitotically active tissues, and the rates and patterns of mutation in post-mitotic tissues.

Mutation burden in stem and differentiated cells

Owing to technical limitations, most of our knowledge of somatic mutagenesis is restricted to stem or proliferating cells. However, as stem cells are believed to be better protected against mutations[25], differentiated cells could conceivably have higher mutational loads and undescribed mutational signatures[14].

We first addressed this question in the haematopoietic system, comparing mature granulocytes to haematopoietic stem and multipotent progenitor cells (HSC/MPPs) (Methods). The haematopoietic system is organized hierarchically, with a heterogeneous pool of slow-cycling stem cells sustaining the production of large numbers of differentiated cells through the extensive proliferation of intermediate progenitor cells (Fig. 2a). HSCs are estimated to divide around once a year and

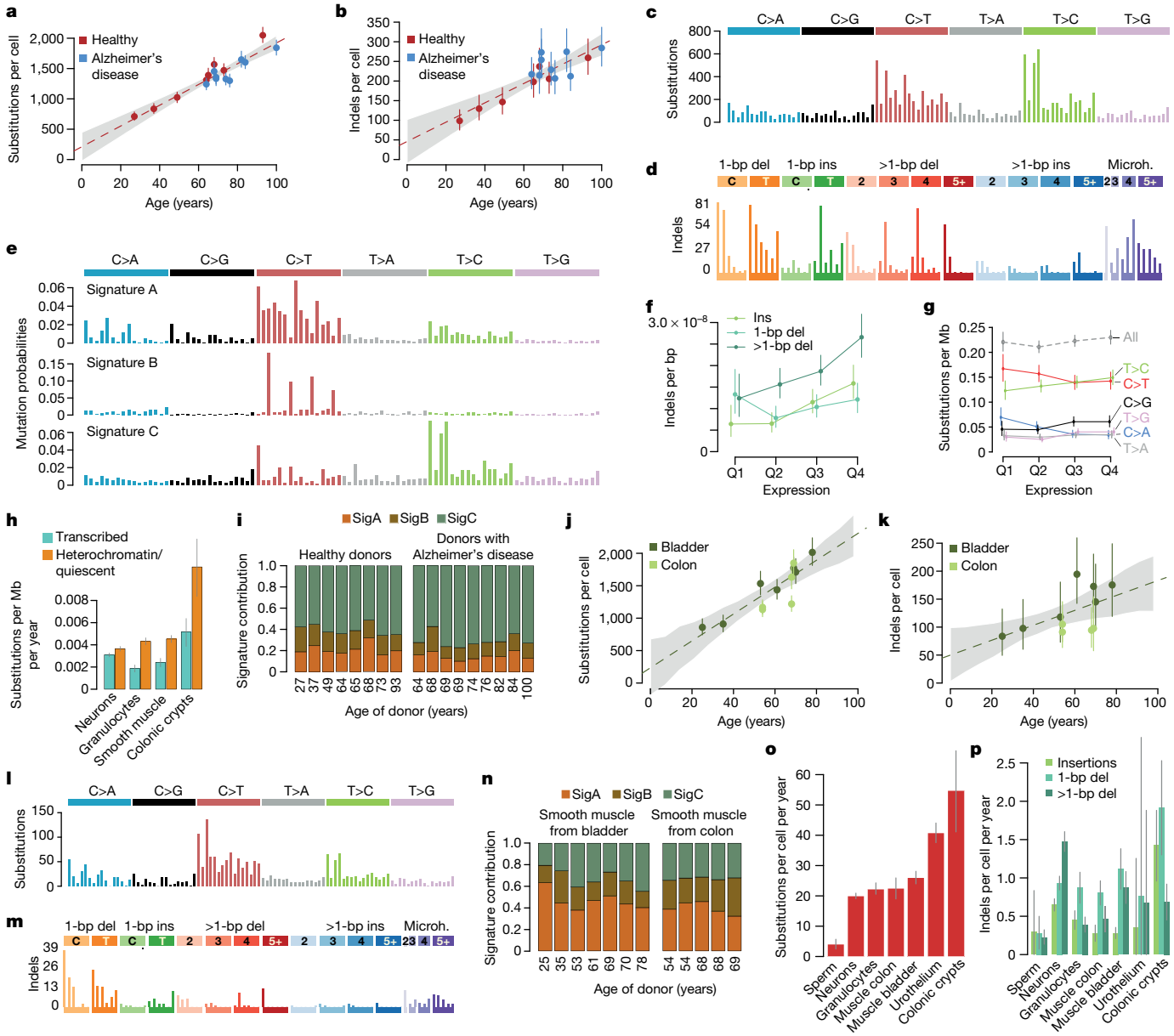

Fig. 3 | Mutational landscape in neurons and smooth muscle. **a**, **b**, Accumulation of substitutions (**a**) and indels (**b**) in neurons throughout life for healthy donors ($n = 8$) and individuals with Alzheimer's disease ($n = 9$). **c**, **d**, Substitution (**c**) and indel (**d**) spectra in neurons; a description of each type of indel can be found in Extended Data Fig. 5d. **d**, $n = 1{,}550$ indels. Microh., microhomology. **e**, Signature decomposition. **f**, **g**, Indel (**f**) and substitution (**g**) rates in genes in the whole cohort by level of expression. Q1–Q4 are ordered in order of increasing expression. **h**, Substitution rates in transcribed (E4 and E5 chromatin states) and inactive (quiescent and heterochromatin, E9 and E15 chromatin states) genomic regions across different cell types (spectra in Extended Data Fig. 8a). **i**, Contribution of signatures A, B and C in neurons. **j**, **k**, Substitutions (**j**) and indels (**k**) per cell in smooth muscle from 10 donors spanning different ages ($n = 2$ libraries for donors aged 54 and 68 years). **l**, **m**, Substitution (**l**) and indel (**m**) spectra in smooth muscle. **m**, $n = 303$ indels. **n**, Exposure to signatures A, B and C in smooth muscle samples. **o**, **p**, Substitution (**o**) and indel (**p**) accumulation per year across different cell types; 95% confidence intervals estimated through simple (neurons and urothelium) or mixed-effect (rest) linear regression with intercept = 0; vertical lines show regression 95% confidence intervals. **a**, **b**, **f**–**h**, **j**, **k**, Vertical lines show Poisson 95% confidence intervals. **a**, **b**, Linear regression models are shown as dashed lines, showing 95% confidence interval as grey areas. **j**, **k**, Linear mixed-effect regressions are shown as dashed lines, showing 95% confidence intervals obtained through parametric bootstrapping (Methods) as grey areas. Regression results with free or zero intercept are provided in Supplementary Table 8.

conservative estimates suggest that an average of over 28 cell divisions must separate stem cells from differentiated cells to explain the production of around 10^{14} mature cells per year (Fig. 2a and Supplementary Note 9). As a result, a considerably higher mutation burden and mutational signatures associated with the proliferation of progenitors may be expected in granulocytes.

We used NanoSeq to sequence 18 samples of granulocytes from 9 healthy donors, who were between 20 and 80 years of age (Supplementary Tables 1, 2). We compared these data to standard whole-genome sequencing of 60 single-cell-derived HSC/MPP colonies from 6 donors (Extended Data Fig. 6a and Supplementary Tables 1, 2) and published data from 110 colonies from 1 donor[26] (Methods). These data revealed remarkably similar mutation burdens in terminally differentiated granulocytes and HSC/MPPs (Fig. 2b). Linear mixed-effect regression yielded indistinguishable slopes for HSC/MPP colonies and granulocytes ($P = 0.92$), with a joint estimate of 19.9 mutations per year (95% confidence interval, 18.3–21.4) (Methods and Supplementary Table 8). The excess of mutations in granulocytes compared with

HSC/MPPs was estimated to be around 51 mutations and not significantly different from zero (95% confidence interval, −14–120, $P = 0.13$) (Methods and Supplementary Table 8). Their mutational spectra were also largely similar (cosine similarity 0.98) (Fig. 2c).

The observation that a considerable increase in cell divisions does not cause a proportional increase in mutation burden suggests that replication errors cannot be responsible for more than a small minority of mutations in HSC/MPPs (Supplementary Note 9). A caveat for this comparison is that HSC/MPP colonies that have successfully been grown in vitro may not reflect the mutation rate of the more quiescent HSCs that are responsible for the long-term maintenance of the haematopoietic system. However, a similar conclusion can be drawn from the granulocyte data alone. The strong linear relationship with age and the small intercept for granulocytes alone (142.1 mutations, 95% confidence interval, −115.3–414.2, compared to the slope of around 19.8 mutations per year) suggest that the majority of the mutations observed in adult granulocytes accumulated in the stem cells responsible for long-term maintenance, and that only a small minority of mutations are accrued during transient proliferation and terminal differentiation (Supplementary Note 9).

To extend the comparison of stem cells and differentiated cells to another tissue with a well-understood stem cell organization, we then studied colonic epithelium. Estimates of the somatic mutation rate in colonic stem cells are available from whole-genome sequencing of clonal organoids derived from single LGR5$^+$ cells[10] and from sequencing single laser-microdissected colonic crypts[6], which over time become clonally derived from a single stem cell[27]. For three previously studied donors, we compared standard whole-genome sequencing of microdissected colonic crypts[6] to NanoSeq data from single crypts or groups of crypts (Extended Data Fig. 6b, c). This revealed similar estimates of mutation burden, despite the time lag to clonality in standard sequencing of colonic crypts (Fig. 2d). Mutation burden and signatures from differentiated cells in colonic epithelium were consistent with those found by previous studies on colonic stem cells, with a dominance of SBS1 and SBS5 signatures[6], and—in some donors—a colibactin signature[28] (Fig. 2e and Extended Data Fig. 6d).

Overall, NanoSeq data on granulocytes and colonic epithelium yielded similar mutation burdens and signatures to their corresponding stem cells. Although larger studies will be needed to identify subtler differences and to address this question in other cell types, these results provide an early view into the somatic mutation landscape of two differentiated cell types.

Mutagenesis in neurons and smooth muscle

Cortical neurons are a notable example of a post-mitotic tissue. This makes them not only a key cell type to study somatic mutagenesis in the absence of cell division, but also inaccessible to traditional sequencing methods. Despite technical challenges hindering progress, somatic mutations in neurodegeneration have attracted considerable interest[1,12,13,29].

We applied NanoSeq to frontal cortex neurons from eight healthy donors and nine patients with Alzheimer's disease (Supplementary Table 1), using nuclei sorting with the neuronal marker NeuN (also known as RBFOX3) (Methods and Extended Data Fig. 7a). These data revealed a linear accumulation of 17.1 substitutions (linear regression, 95% confidence interval, 13.7–20.5) and 2.5 indels (95% confidence interval, 1.7–3.3) per year, approximately constant throughout life (Fig. 3a, b and Supplementary Table 8). This confirms that mutations accumulate in a clock-like manner in cortical neurons in the absence of cell division, consistent with observations from single-cell sequencing[13].

A previous study using single-cell sequencing, with error correction based on single-nucleotide polymorphism (SNP) phasing, reported three signatures in neurons, one that increased linearly with age and two that did not[13]. The spectrum found by NanoSeq and the mutation rate per year closely resemble the age-associated signature in that study (cosine similarity 0.96) (Fig. 3a, c and Extended Data Fig. 7b, c). The two other signatures, responsible for around 72% of all mutations reported in the study[13] (Extended Data Fig. 7d), appear exclusively in single-cell data and probably derive from amplification errors or transient DNA damage. Consistent with this possibility, the dominant signature in single-neuron data closely resembles a single-cell-specific signature reported in vitro[16] (cosine similarity 0.97) (Extended Data Fig. 7b).

To better understand the mutational processes that are active in post-mitotic neurons, we performed signature decomposition on NanoSeq data from neurons, granulocytes, colonic crypts and smooth muscle (described below). Three signatures were extracted (Fig. 3e): signatures A and C imperfectly resembled SBS5 (cosine similarity 0.80) and SBS16 (0.78), respectively, whereas signature B closely matched SBS1 (C>T changes at CpG dinucleotides, cosine similarity 0.96). It is conceivable that SBS5, which appears to be a ubiquitous signature in normal tissues and cancer genomes[30], reflects a collection of co-occurring processes, rather than a single mutational process, leading to some differences across tissues. The observation of signatures that resemble SBS5 and SBS16 in post-mitotic neurons suggests that these common processes—the aetiologies of which remain poorly understood—can occur independently of cell division.

The mutational spectra in neurons (Fig. 3c, d) showed several interesting features. T>C substitutions at ApT sites appear to be enriched in neurons and show strong transcriptional strand biases (Extended Data Fig. 8b, c). Signature B (SBS1), which is believed to be caused by 5-methylcytosine deamination and fixed during DNA replication, accumulates at a low rate with age in neurons (2.5 substitutions per year, linear regression 95% confidence interval, 0.9–4.1; $P = 0.005$) (Extended Data Figs. 7e, 9a, b). This suggests that 5-methylcytosine deamination can be fixed in both DNA strands without cell division, possibly by DNA repair. Neurons also have a higher proportion of indels than other tissues, with an unusual enrichment in indels that are longer than 1 bp in highly expressed genes—a pattern that resembles a mutational process that has recently been described in cancer genomes[31] (Fig. 3d, f and Extended Data Fig. 9c, d). In contrast to other somatic tissues, neurons did not exhibit a clear association between expression levels and substitution rates across genes (Fig. 3g) and the enrichment of mutations in heterochromatin was weaker (Fig. 3h and Extended Data Fig. 8a).

Although the difference is small, neurons from donors with Alzheimer's disease showed a slightly lower substitution rate than those from healthy donors (linear regression, 17.6 (95% confidence interval, 15.0–20.2) versus 19.9 (95% confidence interval, 16.8–23.0) substitutions per year, $P = 0.0029$) (Fig. 3i, Extended Data Fig. 7e and Supplementary Table 8). This could simply reflect differences in the patient cohorts or be related to the pathogenesis of the disease, for example, due to differences in metabolism or variable death rates across subpopulations of neurons in individuals with Alzheimer's disease. Studies with larger cohorts will be required to validate and explain this observation.

To extend these analyses to another tissue that is not amenable to standard sequencing methods, we studied smooth muscle. Visceral smooth muscle cells are thought to divide infrequently in normal conditions[32]. We used laser microdissection of histological sections of bladder and colon to collect smooth muscle from 10 donors (Extended Data Figs. 6b, 10a and Supplementary Tables 1, 2). As expected for a polyclonal tissue, standard whole-genome sequencing detected few mutations and at low allele frequencies in these samples (Methods and Extended Data Fig. 10b, c). By contrast, NanoSeq revealed that the substitution and indel burdens increase linearly with age, with 20.7 substitutions per year per diploid genome (95% confidence interval, 13.7–28.0) and 1.3 indels per year (95% confidence interval, 0.4–2.3) (Fig. 3j, k and Supplementary Table 8). Despite their different anatomical origin, smooth muscle cells from the bladder and colon walls showed relatively similar mutation rates. Overall, the mutational spectrum of smooth muscle shared some similarities with that of granulocytes and neurons (Figs. 1c, 3l–n), with all

three signatures (A–C) accumulating linearly with age (Extended Data Fig. 7f). The smooth muscle spectrum also resembles the mutational spectrum of skeletal muscle satellite cells, which have been studied by in vitro expansion[11] (Supplementary Note 10).

Taken together, granulocytes, smooth muscle and neurons showed more limited variation in mutation rate and spectra across individuals than has been observed in epithelia that are exposed to exogenous mutagens, such as skin[3], colon[6] (Fig. 2c), bronchus[33] or bladder[8,34]. This suggests that the variation in endogenous mutagenesis across individuals is modest, at least in the cohorts studied here.

Discussion

Building on duplex sequencing and BotSeqS, we have developed a sequencing protocol with error rates in single DNA molecules of less than five errors per billion sites. This error rate enables the study of mutation rates and signatures in any human tissue or cell population.

Most of our current knowledge of somatic mutagenesis is restricted to mitotically active cells. We have used the ability to sequence any cell type to study the mutational landscape of non-dividing cells in mitotically active and inactive tissues. A remarkable observation that emerges from these data is that somatic mutation rates vary modestly (around two- to threefold) across a diverse range of somatic cell types, largely independently of cell division rates (Fig. 3o, p and Supplementary Note 9). Indeed, similar mutation rates are found in non-dividing cortical neurons, in smooth muscle and in blood; or in colonic epithelium, which divides every few days, and in mostly quiescent hepatocytes[10] and urothelial cells (Fig. 3o, p).

DNA replication and cell division have long been assumed to be major sources of somatic mutations, either due to DNA polymerase errors or the fixation of unrepaired damage during replication[35]. However, the linear accumulation of somatic mutations in post-mitotic neurons, with similar rates and signatures to some mitotically active tissues, indicates that dominant mutational processes can occur independently of cell division. These mutations may result from the interplay between endogenous DNA damage and repair that occurs in cells at all times. The similar mutation burden and signatures in granulocytes and haematopoietic stem cells, despite a different divisional load, could also be consistent with a time-dependent rather than a division-dependent accumulation of somatic mutations during haematopoiesis. Taken together, division-independent mutational processes may have a larger role in adult mutagenesis than it is commonly assumed.

In addition to enabling studies of somatic mutagenesis in any tissue, the ability to accurately detect mutations in single molecules of DNA has wider applications. NanoSeq could be used for mutagenesis screens and in vitro studies, exposing cell cultures or experimental models to different mutagens and quantifying mutagenesis across the genome and over time, without the need for single-cell bottlenecks[36,37]. Sonication followed by exonuclease digestion opens the door to targeted applications, to study the landscape of driver or pathogenic mutations in polyclonal samples, across tissues and conditions. Being insensitive to clonality, NanoSeq can also be used to efficiently and accurately quantify somatic mutation rates and signatures in non-invasive tissue samples, enabling studies of somatic mutagenesis in large-scale cohorts, across genetic backgrounds, exposures and risk factors, in health and disease.

Online content

Any methods, additional references, Nature Research reporting summaries, source data, extended data, supplementary information, acknowledgements, peer review information; details of author contributions and competing interests; and statements of data and code availability are available at https://doi.org/10.1038/s41586-021-03477-4.

1. Kennedy, S. R., Loeb, L. A. & Herr, A. J. Somatic mutations in aging, cancer and neurodegeneration. *Mech. Ageing Dev.* **133**, 118–126 (2012).
2. Vogelstein, B. et al. Cancer genome landscapes. *Science* **339**, 1546–1558 (2013).
3. Martincorena, I. et al. High burden and pervasive positive selection of somatic mutations in normal human skin. *Science* **348**, 880–886 (2015
4. Martincorena, I. et al. Somatic mutant clones colonize the human esophagus with age. *Science* **362**, 911–917 (2018).
5. Yizhak, K. et al. RNA sequence analysis reveals macroscopic somatic clonal expansion across normal tissues. *Science* **364**, eaaw0726 (2019).
6. Lee-Six, H. et al. The landscape of somatic mutation in normal colorectal epithelial cells. *Nature* **574**, 532–537 (2019).
7. Brunner, S. F. et al. Somatic mutations and clonal dynamics in healthy and cirrhotic human liver. *Nature* **574**, 538–542 (2019).
8. Li, R. et al. Macroscopic somatic clonal expansion in morphologically normal human urothelium. *Science* **370**, 82–89 (2020).
9. Welch, J. S. et al. The origin and evolution of mutations in acute myeloid leukemia. *Cell* **150**, 264–278 (2012).
10. Blokzijl, F. et al. Tissue-specific mutation accumulation in human adult stem cells during life. *Nature* **538**, 260–264 (2016).
11. Franco, I. et al. Somatic mutagenesis in satellite cells associates with human skeletal muscle aging. *Nat. Commun.* **9**, 800 (2018).
12. Lodato, M. A. et al. Somatic mutation in single human neurons tracks developmental and transcriptional history. *Science* **350**, 94–98 (2015).
13. Lodato, M. A. et al. Aging and neurodegeneration are associated with increased mutations in single human neurons. *Science* **359**, 555–559 (2018).
14. Brazhnik, K. et al. Single-cell analysis reveals different age-related somatic mutation profiles between stem and differentiated cells in human liver. *Sci. Adv.* **6**, eaax2659 (2020).
15. Xing, D., Tan, L., Chang, C. H., Li, H. & Xie, X. S. Accurate SNV detection in single cells by transposon-based whole-genome amplification of complementary strands. *Proc. Natl Acad. Sci. USA* **118**, e2013106118 (2021).
16. Petljak, M. et al. Characterizing mutational signatures in human cancer cell lines reveals episodic APOBEC mutagenesis. *Cell* **176**, 1282–1294.e20 (2019).
17. Salk, J. J., Schmitt, M. W. & Loeb, L. A. Enhancing the accuracy of next-generation sequencing for detecting rare and subclonal mutations. *Nat. Rev. Genet.* **19**, 269–285 (2018).
18. Schmitt, M. W. et al. Detection of ultra-rare mutations by next-generation sequencing. *Proc. Natl Acad. Sci. USA* **109**, 14508–14513 (2012).
19. Kennedy, S. R. et al. Detecting ultralow-frequency mutations by duplex sequencing. *Nat. Protocols* **9**, 2586–2606 (2014).
20. Hoang, M. L. et al. Genome-wide quantification of rare somatic mutations in normal human tissues using massively parallel sequencing. *Proc. Natl Acad. Sci. USA* **113**, 9846–9851 (2016).
21. You, X. et al. Detection of genome-wide low-frequency mutations with paired-end and complementary consensus sequencing (PECC-seq) revealed end-repair-derived artifacts as residual errors. *Arch. Toxicol.* **94**, 3475–3485 (2020).
22. Costello, M. et al. Discovery and characterization of artifactual mutations in deep coverage targeted capture sequencing data due to oxidative DNA damage during sample preparation. *Nucleic Acids Res.* **41**, e67 (2013).
23. Kong, A. et al. Rate of de novo mutations and the importance of father's age to disease risk. *Nature* **488**, 471–475 (2012).
24. Rahbari, R. et al. Timing, rates and spectra of human germline mutation. *Nat. Genet.* **48**, 126–133 (2016).
25. Wyles, S. P., Brandt, E. B. & Nelson, T. J. Stem cells: the pursuit of genomic stability. *Int. J. Mol. Sci.* **15**, 20948–20967 (2014).
26. Lee-Six, H. et al. Population dynamics of normal human blood inferred from somatic mutations. *Nature* **561**, 473–478 (2018).
27. Nicholson, A. M. et al. Fixation and spread of somatic mutations in adult human colonic epithelium. *Cell Stem Cell* **22**, 909–918.e8 (2018).
28. Pleguezuelos-Manzano, C. et al. Mutational signature in colorectal cancer caused by genotoxic pks$^+$ *E. coli*. *Nature* **580**, 269–273 (2020).
29. Poduri, A., Evrony, G. D., Cai, X. & Walsh, C. A. Somatic mutation, genomic variation, and neurological disease. *Science* **341**, 1237758 (2013).
30. Alexandrov, L. B. et al. The repertoire of mutational signatures in human cancer. *Nature* **578**, 94–101 (2020).
31. Rheinbay, E. et al. Analyses of non-coding somatic drivers in 2,658 cancer whole genomes. *Nature* **578**, 102–111 (2020).
32. Gabella, G. Cells of visceral smooth muscles. *J. Smooth Muscle Res.* **48**, 65–95 (2012).
33. Yoshida, K. et al. Tobacco smoking and somatic mutations in human bronchial epithelium. *Nature* **578**, 266–272 (2020).
34. Lawson, A. R. J. et al. Extensive heterogeneity in somatic mutation and selection in the human bladder. *Science* **370**, 75–82 (2020).
35. Gao, Z., Wyman, M. J., Sella, G. & Przeworski, M. Interpreting the dependence of mutation rates on age and time. *PLoS Biol.* **14**, e1002355 (2016).
36. Kucab, J. E. et al. A compendium of mutational signatures of environmental agents. *Cell* **177**, 821–836 (2019).
37. Matsumura, S. et al. Genome-wide somatic mutation analysis via Hawk-seq™ reveals mutation profiles associated with chemical mutagens. *Arch. Toxicol.* **93**, 2689–2701 (2019).

Methods

Data reporting

No statistical methods were used to predetermine sample size. The experiments were not randomized and the investigators were not blinded to allocation during experiments and outcome assessment.

Sample collection and ethics

All samples were collected with informed consent from all human research participants or their families. The haematological samples used in the study were obtained from the Cambridge Blood and Stem Cell Biobank, the Cambridge Biorepository for Translational Medicine and the Cambridge Bioresource (REC references: 07-MRE05-44, 18/EE/0199, 15/EE/0152, NRES Committee East of England, Cambridge South). Sperm samples were collected under REC ethics approval EC04/015, London, Westminster REC and 16/NE/003, NRES Committee North East-Newcastle and North Tyneside 1. Colon and bladder tissue were collected by the Cambridge Biorepository for Translational Medicine (REC reference: 15/EE/0152, NRES Committee East of England, Cambridge South). Frozen biopsies of frontal cortex from healthy donors and individuals with Alzheimer's disease were collected by the Cambridge Brain Bank (Supplementary Tables 1, 2; REC ethics approval: 10/H0308/56, East of England, Nottingham).

Sorting, colony growth and mutation calling of granulocytes and HSC/MPP colonies

We use two different terms to refer to colonies derived from HSCs or progenitor cells, depending on the membrane markers used for cell sorting: HSPCs (haematopoietic stem and progenitor cells), which comprise $CD34^+$ pools, and HSC/MPPs, which are $CD34^+CD38^-CD45RA^-$ cells.

A sample of granulocytes from a 59-year-old male donor (PD43976_59yo) from whom 110 HSPC colonies were available[26] was used for the initial validation of the BotSeqS and NanoSeq protocols (Supplementary Tables 1, 2). To estimate the NanoSeq error rate, cord-blood granulocytes from two neonatal donors were sequenced by NanoSeq and the mutation burdens and spectra were compared to those from 50 HSC/MPP colonies per donor. For the comparison of differentiated and stem cells, NanoSeq data from granulocytes from 9 donors of different ages were compared to standard sequencing of single-cell-derived HSC/MPP colonies from 6 donors (10 HSC/MPP colonies per donor) and 110 HSPC colonies that were already available from a 59-year-old donor[26]. These 110 HSPC colonies included 67 HSC/MPPs, 32 megakaryocyte–erythrocyte progenitors, 7 granulocyte–macrophage progenitors and 4 common myeloid progenitors.

For PD43976_59yo, HSPC colonies were grown and mutations called as described previously[26]. For the remaining donors, whole blood was diluted with PBS and mononuclear cells were isolated using lymphoprep (STEMCELL Technologies) density-gradient centrifugation. The mononuclear cell fraction was then removed and added to a fresh tube, leaving behind the red blood cell pellet, which also contained the granulocyte fraction. The mononuclear cell fraction was depleted of red blood cells by a single 15-min incubation with RBC lysis buffer (BioLegend) at 4 °C. Granulocytes were purified from the red blood cell pellets using 3 incubations (for 20 min, 10 min and 10 min) with RBC lysis buffer (BioLegend) at room temperature. $CD34^+$ selection of peripheral blood and cord blood samples was done using the EasySep human whole-blood CD34-positive selection kit (Stem Cell Technologies) according to the manufacturer's instructions. Bone marrow samples did not undergo $CD34^+$ selection before sorting.

Mononuclear cells or CD34-enriched samples were centrifuged and resuspended in PBS and 3%FBS containing an antibody panel consisting of (antibody/fluorochrome): CD3/FITC (1:500), CD90/PE (1:50), CD49f/PECy5 (1:100), CD38/PECy7 (1:100), CD19/A700 (1:300), CD34/APC Cy7 (1:100), CD45RA/BV421 (1:100) and Zombie/Aqua (1:2,000).

Cells were stained (30 min at 4 °C) in the dark before washing, centrifugation (500*g* at room temperature) and resuspension in PBS and 3%FBS for cell sorting. Index sorting of 'HSC/MPP pool' cells was performed on a BD AriaIII Cell Sorter (BD Biosciences) at the NIHR Cambridge BRC Cell Phenotyping Hub, as per the gating structure shown in Extended Data Fig. 6a ($CD34^+$, $CD38^-$ and $CD45RA^-$).

'HSC/MPP pool' cells were single-cell-sorted into Nunc 96-well flat-bottomed tissue-culture plates (ThermoFisher) containing 100 µl supplemented StemPro medium (Stem Cell Technologies). MEM medium contained StemPro nutrients (0.035%, Stem Cell Technologies), L-glutamine (1%, ThermoFisher), penicillin–streptomycin (1%, ThermoFisher) and cytokines (SCF, 100 ng ml^{-1}; FLT3, 20 ng ml^{-1}; TPO, 100 ng ml^{-1}; EPO, 3 ng ml^{-1}; IL-6, 50 ng ml^{-1}; IL-3, 10 ng ml^{-1}; IL-11, 50 ng ml^{-1}; GM-CSF, 20 ng ml^{-1}; IL-2, 10 ng ml^{-1}; IL-7, 20 ng ml^{-1}; lipids, 50 ng ml^{-1}) to promote differentiation towards myeloid/erythroid/megakaryocyte and NK lineages. Manual assessment of colony growth was made at 14 days. Colonies were topped up with an additional 50 µl MEM medium on day 15 if the colony was ≥1/4 the size of the well. Following 21 ± 2 days in culture, colonies were selected by size criteria. Colonies of ≥3,000 cells in size were collected into a U-bottomed 96-well plate (ThermoFisher). Plates were then centrifuged (500*g* for 5 min), the medium was discarded, and the cells were resuspended in 50 µl PBS before freezing at −80 °C. Colonies of <3,000 cells but >200 cells in size were collected into 96-well skirted LoBind plates (Eppendorf) and centrifuged (800*g* for 5 min). The supernatant was removed leaving 5–10 µl using an aspirator before DNA extraction of the fresh cell pellet.

DNA extraction was performed using the DNeasy 96 Blood and Tissue kit (Qiagen) for larger HSC colonies, or the Arcturus Picopure DNA Extraction kit (ThermoFisher) for smaller HSC colonies. Both kits were used according to the manufacturer's instructions. Extracted DNA (1–5 ng) from each colony was processed using a recently developed low-input enzymatic fragmentation-based library preparation method[38]. All samples were subjected to whole-genome sequencing at 8–35× coverage on either the HiSeq X or the NovaSeq (Illumina) platforms to generate 150-bp paired-end reads. BWA-MEM was used to align sequences to the human reference genome (NCBI build37).

Sperm samples

DNA was extracted from sperm samples from two donors, aged 21 and 73 years, and sequenced using the NanoSeq protocol. Because of the low mutation burden of the germline, we sequenced 7 separate aliquots of sperm DNA from the 21-year-old donor to estimate the error rate of the NanoSeq protocol (Supplementary Tables 1, 2).

Laser microdissection of colonic crypts, and bladder and colon smooth muscle

Colon and bladder biopsies were obtained from organ donors who are deceased (ranging in age from 25 to 78 years; Supplementary Table 1). Different microbiopsies from these specimens have been used in previously published studies[6,34,39].

Colon biopsies were fresh-frozen at the time of collection and stored at −80 °C. The colon biopsies subsequently underwent formalin-free fixation for 24 h in PAXgene Tissue Fix containers (PreAnalytiX) before being transferred to PAXgene STABILIZER solution (PreAnalytiX). Bladder biopsies underwent formalin-free fixation at the time of collection and were stored at −20 °C as previously described[38].

Before laser-capture microdissection, samples were processed, embedded in paraffin and sectioned as described previously[34]. Microbiopsies were dissected using an LMD7 microscope (Leica Microsystems). Examples of microdissected regions for both specimen types can be found in Extended Data Figs. 6, 10. Proteolysis of isolated regions was performed using an Arcturus PicoPure DNA Extraction Kit (Thermo Fisher Scientific). Cell lysate was stored at −20 °C before library preparation.

Neuronal nuclei sorting from frontal cortex samples

Neuronal nuclei were isolated, stained and extracted from the frontal cortex samples as described previously[40] using frozen biopsies of frontal cortex from eight healthy donors and nine individuals with Alzheimer's disease. In brief, small cuts of 1–2 mm were taken from fresh-frozen samples. Dounce homogenization was then used to free nuclei before filtration, density centrifugation and immunostaining. Samples were stained using DAPI (ThermoFisher, D1306) and Milli-Mark anti-NeuN-PE antibody (1:500; MilliPore, FCMAB317PE). The immunostained samples were then sorted using FACS as per the gating strategy in Extended Data Fig. 7a. Then, 15,000 nuclei were collected in 20 µl of the Arcturus PicoPure DNA Extraction Kit (Thermo Fisher Scientific) before undergoing digestion. Nuclear lysate was then stored at −20 °C before library preparation.

The distributions of NeuN-PE intensities in most samples revealed a bimodal distribution. As a quality control, we fitted a mixture model of two Gamma distributions to the NeuN-PE intensities for every sample. Only samples with tenfold (1 $\log_{10}$-transformed unit) separation between the mean of both peaks were considered for analysis, which led to the exclusion of an outlier sample.

BotSeqS and NanoSeq library preparation protocols

BotSeqS libraries shown in Fig. 1 and Extended Data Fig. 3 were prepared as follows. The DNA was sheared to 450 bp using a Covaris. Sonicated DNA was quantified and 50 ng was used as input into end repair using the NEBNext Ultra End Repair/dA-Tailing Module (NEB E7442S). The DNA was cleaned using a 2.5× Ampure XP (Beckman Coulter) bead ratio and eluted in 12 µl nuclease-free water (NFW). Subsequently, 10 µl of the elution product was taken and added to the ligation reaction, which consisted of 3.74 µl NEBuffer 4, 3.74 µl 10 mM ATP, 0.33 µl xGen Duplex Seq Adapters (Integrated DNA Technologies (IDT), 1080799), 0.56 µl T4 DNA ligase (NEB, M0202L) and 19.03 µl NFW. The reaction was incubated at 20 °C for 20 min. The DNA was cleaned up using 37.4 µl Ampure XP beads and the DNA was eluted in 50 µl NFW. Libraries were quantified (using quantitative PCR (qPCR)) and amplified following the NanoSeq protocol. For the BotSeqS data on granulocytes from a 59-year-old donor (Extended Data Figs. 1, 2), we used a previous implementation of the protocol, as follows: 10 ng of sonicated DNA was end-repaired and ligated using the NEBNext Ultra II kit (New England Biolabs (NEB)) and 0.66 µl 1.5 µM xGen Duplex Seq Adapters - Tech Access (IDT, 1080799).

NanoSeq libraries were prepared as follows: genomic DNA or lysed tissue microbiopsies in 20 µl of buffer were purified using 100 µl of a 50:50 water:AMPure XP bead mixture and eluted in 20 µl NFW. Then, 20 µl of the bead suspension was taken forward into an on-bead fragmentation reaction. Fragmentation occurred in a final volume of 25 µl including 2.5 µl 10× CutSmart buffer (500 mM potassium acetate, 200 mM Tris-acetate, 100 mM magnesium acetate, 1 mg ml^{-1} BSA, pH 7.9 at 25 °C), 0.5 µl 5 U µl^{-1} HpyCH4V (Supplementary Note 2) and 2 µl NFW. Fragmentation reactions were incubated at 37 °C for 15 min, purified with 2.5× AMPure XP beads and resuspended in 15 µl NFW. Fragmented DNA was A-tailed in 15 µl reactions including 10 µl fragmentation product, 1.5 µl 10× NEBuffer 4 (500 mM potassium acetate, 200 mM Tris-acetate, 100 mM magnesium acetate, 10 mM DTT, pH 7.9 at 25 °C), 0.15 µl 5 U µl^{-1} Klenow fragment (3′ to 5′ exo-, NEB), either 1.5 µl 1 mM dATP or 1.5 µl 1 mM equimolar dATP/ddBTPs (Supplementary Note 3) and 1.85 µl NFW. ddBTPs here refer to ddTTP, ddCTP and ddGTP. Reactions were incubated at 37 °C for 30 min. The 15-µl A-tailing reaction product was added to 22.4 µl ligation mix, which consisted of 2.24 µl 10× NEBuffer 4, 3.74 µl 10 mM ATP, 0.33 µl 15 µM xGen Duplex Seq Adapters (IDT, 1080799), 0.56 µl 400 U µl^{-1} T4 DNA ligase (NEB) and 15.53 µl NFW. Reactions were incubated at 20 °C for 20 min and subsequently purified with 1× AMPure XP beads and resuspended in 50 µl of NFW.

Mung Bean NanoSeq libraries were prepared as follows: DNA was sheared to an average size of 450 bp using focused ultrasonication (Covaris 644 LE220). Sheared DNA was quantified and 50 ng was used as input per reaction. Mung Bean nuclease (NEB, M0250S) was diluted to 1 U µl^{-1}, 0.5 U µl^{-1} or 0.25 U µl^{-1} in 1× Mung Bean nuclease buffer. The Mung Bean reaction was carried out in a final volume of 30 µl including 2.9 µl 10× Mung Bean nuclease buffer, 1 µl diluted Mung Bean nuclease, 10 µl DNA and 16.1 µl NFW. The reaction was incubated at 30 °C for 30 min. Then, 1 µl 0.3% SDS was added and the reaction was cleaned up using 77.5 µl Ampure XP beads. Samples were eluted in 12 µl NFW. Then, 10 µl was used as input into a phosphorylation reaction by adding 1.5 µl NEBuffer 4 (NEB, B7004S), 1.5 µl 10 mM ATP (Fisher Scientific 10304340), 0.6 µl T4 Polynucleotide Kinase (NEB, M0201S) and 1.4 µl NFW. The reaction was incubated at 37 °C for 30 min. Next, 13 µl was taken forward into an A-tailing reaction, adding 0.2 µl NEBuffer 4, 1.5 µl 1 mM dATP/ddBTP (NEB, N0440S/GE Healthcare, 27204501), 0.15 µl Klenow fragment (3′ to 5′ exo-, NEB, M0212L) and 0.15 µl NFW. The reaction was incubated at 37 °C for 30 min. The whole sample of 15 µl was taken into the ligation reaction mix, which consisted of 2.24 µl NEBuffer 4, 3.74 µl 10 mM ATP, 0.33 µl xGen Duplex Seq Adapters (IDT, 1080799), 0.56 µl T4 DNA ligase (NEB, M0202L) and 15.53 µl NFW. The reaction was incubated at 20 °C for 20 min. The DNA was cleaned up using 37.4 µl Ampure XP beads and DNA was eluted in 50 µl NFW. Libraries were quantified and amplified following the NanoSeq protocol.

DNA quantification, dilution and PCR amplification

DNA was quantified by qPCR using a KAPA library quantification kit (KK4835). The supplied primer premix was first added to the supplied KAPA SYBR FAST master mix. In addition, 20 µl of 100 µM NanoqPCR1 primer (HPLC, 5′-ACACTCTTTCCCTACACGAC-3′) and 20 µl of 100 µM NanoqPCR2 primer (HPLC, 5′-GTGACTGGAGTTCAGACGTG-3′) were added to the KAPA SYBR FAST master mix. Samples were diluted 1:500 using NFW and reactions were set up in a 10-µl reaction volume (6 µl master mix, 2 µl sample/standard, 2 µl water) in a 384-well plate. Samples were run on the Roche 480 Lightcycler and analysed using absolute quantification (second derivative maximum method) with the high sensitivity algorithm. The concentration (nM (fmol µl^{-1})) was determined as follows: mean of sample concentration × dilution factor (500) × 452/573/1,000 (where 452 is the size of the standard in bp and 573 is the proxy for the average fragment length of the library in bp), and multiplied by an adjustment factor of 1.5. Samples were diluted to the desired fmol amount (typically 0.3 fmol for a 15× run) in 25 µl using NFW.

Libraries were subsequently PCR-amplified in a 50-µl reaction volume comprising 25 µl sample, 25 µl NEBNext Ultra II Q5 Master Mix and unique dual index (UDI) containing PCR primers (dried). The reaction was cycled as follows: step 1, 98 °C 30 s; step 2, 98 °C 10 s; step 3, 65 °C 75 s; step 4, return to step 2 13 times; step 5, 65 °C for 5 min; step 6, hold at 4 °C. The number of PCR cycles is dependent on the input: 0.1 fmol, 16 cycles; 0.3 fmol, 14 cycles; 0.6 fmol, 13 cycles; 5 fmol, 10 cycles.

The PCR product was subsequently cleaned up using two consecutive 0.7× AMPure XP clean-ups. Each sample was quantified using the AccuClear Ultra High Sensitivity dsDNA Quantification kit (Biotium) and pooled. Libraries were sequenced on Illumina sequencing platforms such as NovaSeq using 150-bp paired-end reads.

Library dilution and sequencing efficiency

The efficiency and cost effectiveness of duplex sequencing depends on optimizing the duplicate rate to maximize the number of read bundles (defined as a family of PCR duplicates) with at least two duplicate reads from each original strand. Duplicate rates that are too high result in few read bundles of unnecessarily large sizes, whereas duplicate rates that are too low result in many read bundles with few having two or more read pairs from each strand.

To maximize the efficiency of the protocol, we studied analytically and empirically the relationship between the number of DNA molecules in the library (library complexity) and the resulting duplicate rate as a function of the number of read pairs sequenced. We found

that optimal duplicate rates and optimal efficiency can be ensured across a wide range of samples. If we assume negligible PCR biases, with copies from all original ligated DNA fragments represented in equimolar amounts in the amplified library, the bundle size distribution of observed reads can be modelled as a zero-truncated Poisson distribution. Let r (sequence ratio) be the ratio between the number of sequenced reads and the number of amplifiable DNA fragments in the original library. The mean read bundle size (m) can then be estimated as the mean of the zero-truncated Poisson distribution: . This parameter then enables a simple estimation of the duplicate rate of a library (d, defined as the fraction of reads that are duplicate copies, and identified as reads having the same barcodes and the same 5′ and 3′ coordinates):

$$d = \frac{m-1}{m} = 1 - \frac{1}{m} = 1 - \frac{1-e^{-r}}{r}$$

We can define the efficiency of a duplex sequencing library (E) as the ratio between the number of base pairs with duplex coverage (bundles with ≥2 reads from both strands) and the number of base pairs sequenced. This can be modelled as:

$$E = \frac{P\left(x \geq 2; \frac{r}{2}\right)^2}{m}$$

where the numerator is the probability of a read bundle having at least two reads from both strands (that is, usable bundles), based on the zero-truncated Poisson distribution (denoted as P), and the denominator is the sequence investment in each read bundle (that is, the average read bundle size). On the basis of this equation, we can estimate numerically that the optimal duplicate rate is around 81% (Extended Data Fig. 4a and in the supplementary code repository (https://zenodo.org/record/4604537)) and that duplicate rates between 65% and 90% would yield ≥80% of the maximum attainable efficiency. In terms of r, the optimum r is 5.1 read pairs sequenced per original DNA fragment (r_{opt}), with values between 2.7 and 9.6 yielding ≥80% of the maximum efficiency. Knowing the concentration of a NanoSeq (or BotSeqS) library in fmol μl^{-1} (estimated using a qPCR reaction on an aliquot of the library), we can use r_{opt} to calculate the volume of library that needs to be amplified to yield optimal duplicate rates (that is, maximum duplex efficiency), as a function of the desired amount of raw sequencing:

$$\text{fmol}_{opt} = \frac{N}{f\, r_{opt}}$$

Here, N is the number of paired-end reads that will be sequenced and f is the number of DNA fragments per fmol of library (referring specifically to ligated and amplifiable fragments within the size-selection range). Using an initial set of libraries, we compared a range of library inputs (fmol) to the estimated number of unique molecules in the library inferred from the sequencing data (using Piccard's software). This analysis revealed that, for our choice of restriction enzyme and size-selection conditions, f approximately equated to 10^8 fragments per fmol.

Using the above equation, we can optimize the efficiency of NanoSeq independently of the input amount of DNA in a given sample. For example, around 0.3 fmol of library yields optimal duplicate rates when sequencing 150 million 150-bp paired-end reads, which are the equivalent to around 15× coverage in standard human whole-genome sequencing. Approximately 0.6 fmol yields optimal efficiency when sequencing 300 million reads (equivalent to 30× whole-genome coverage). Note that, as predicted by the equations above, deviations of around twofold from r_{opt} still yield high efficiency. Using these equations, we reliably obtained near-optimal duplicate rates from a wide range of samples (Extended Data Fig. 4 and Supplementary Table 2). Overall, we found that 30× of standard sequencing output (300×10^6 150 bp paired-end reads) yielded approximately 3 Gb of high-accuracy duplex coverage (a haploid genome equivalent) after application of all computational filters.

Our choices of restriction enzyme and size selection restrict the coverage to around 30% of the human genome. Although the covered regions are sufficiently diverse to enable unbiased estimates of burden and signatures (Methods), applications that require full-genome coverage, such as targeted sequencing, would require alternative fragmentation strategies. One option may be exonuclease blunting after sonication, instead of end repair. Nevertheless, for the study of burden and signatures, the use of restriction enzymes has two notable advantages. First, this protocol is able to work with very low inputs of DNA. We estimated library yields for a range of input DNA amounts (Extended Data Fig. 4b) and found that the minimum DNA input required to obtain 0.3 fmol for a 15× run (corresponding to about 1.5–3 Gb of effective duplex coverage) was around 1 ng of input DNA. This low-input requirement enables the application of NanoSeq to microscopic areas of tissue (as shown for colonic crypts and smooth muscle) and to rare cell populations using flow sorting. A second advantage is that, since coverage is concentrated to approximately 30% of the human genome, matched normal samples can be sequenced at lower cost by using undiluted NanoSeq libraries (≥3 fmol of library sequenced at 8× genome equivalent is enough to provide over 20× matched normal coverage in the 30% of informative genome).

Sequencing, preprocessing and filtering of BotSeqS and NanoSeq libraries

Standard sequencing matched-normal libraries were aligned to the human reference genome (GRCh37, hs37d5 build) using BWA-MEM v.0.7.5a-r405[41] with default parameters. Alignments were sorted by coordinate and read duplicates were marked using biobambam2[42] v.2.076 bamsormadup. Matched normal reads were filtered if marked as duplicate, supplementary, QC fail, unmapped or secondary alignments. For some samples, as described above, instead of standard whole-genome sequencing, we used undiluted NanoSeq libraries (typically around 5 fmol) as matched normal samples, reducing the costs of sequencing matched normal samples.

NanoSeq and BotSeqS libraries were sequenced using 150-bp paired-end reads on HiSeq2500, HiSeqX and NovaSeq platforms.

NanoSeq sequencing reads begin with adaptor sequences: NNNT or NNNXT for BotSeqS libraries and NNNTCA or NNNXTCA for HpyCH4V libraries (HpyCH4V cuts at TGCA motifs). NNN is a random three nucleotide barcode, T is the adaptor overhang and X is a 'spacer' nucleotide designed to increase nucleotide diversity in the sequencing run. We used a custom Python script to process demultiplexed fastq files by extracting the three-nucleotide barcode, clipping the remaining adaptor bases (two bases for BotSeqS and four bases for NanoSeq libraries) and appending barcode sequences to the fastq header. Barcodes with non-canonical bases (not A, C, G or T) were filtered out. Reads were aligned to hs37d5 using BWA-MEM (v.0.7.5a-r405), using the -C option to append barcode sequences to alignments. Alignments were sorted by coordinate, duplicates were marked and reads were annotated with read coordinate, mate coordinate and optical duplicate auxiliary tags using biobambam2 v.2.076 bamsormadup and bammarkduplicatesopt (optminpixeldif = 2500). Reads were filtered when they were not marked as proper pairs or were marked as optical duplicate, supplementary, QC fail, unmapped or secondary alignments. Each read was marked with an auxiliary tag comprising the reference name, the read pair mapping coordinates and their barcodes.

Consensus base quality scores

Bayes' theorem was used to compute the posterior probability of each base call B given the pileup of reads D from one strand of a template molecule at one genomic position. There are four possible genotypes $i \in$ (A, C, G, T). The posterior probability is calculated using:

$$P(B|D) = \frac{P(B)P(D|B)}{\sum_i P(B_i)P(D|B_i)}$$

Under a uniform prior, where any of the four possible genotypes are equally likely, the equation can be simplified to:

$$P(B|D) = \frac{P(D|B)}{\sum_i P(D|B_i)}$$

To calculate $P(D|B)$, information is integrated from reads in D, where $b_j \in$ (A, C, G, T) is the base of read $j = 1 \ldots d$:

$$P(D|B_i) = \prod_{j=1}^{j=d} P(b_j|B_i)$$

To calculate $P(b_j|B_i)$ we use the probability that base b_j is an error, calculated from its Phred quality score q_j:

$$P(b_j|G_i) = 1 - e_j \text{ if } b_j = B_i, \text{ otherwise } e_j/3$$

where

$$e_j = 10^{\frac{-q_j}{10}}$$

We note that the final probability $P(D|B)$ is the probability that the base call is correct after sequencing and not the probability that the base represents the correct genotype of the original template strand, where independence between observations cannot be assumed. $P(B|D)$ is rescaled into a Phred quality score Q using:

$$Q = -10 \log_{10} P(B|D)$$

In cases in which the two read mates overlap, the consensus base quality is calculated using both forward and reverse reads.

Base calling and filtering

We developed a set of filters that successfully reduced false-positive calls. An important feature of the bioinformatics pipeline is that we apply the same filters to call reference and mutated bases, which enables the direct calculation of mutation rates.

The calling method requires a matched normal to filter out germline SNPs. An additional mask to filter sites that are problematic is also advisable. This matched normal can be obtained by standard protocols or by sequencing undiluted NanoSeq libraries (≥3 fmol), as explained above.

The same filters were applied to NanoSeq and BotSeq data. (1) We require that each read bundle (that is, group of PCR duplicates) has at least two reads from each of the two original DNA strands. (2) The consensus base quality score should be at least 60 (this guarantees that there is strong support for a given base call from the duplicate reads that form a read bundle). (3) The minimum difference between the primary alignment score (AS) and the secondary alignment score (XS) should be higher than 50, to keep only read pairs with unambiguous mapping (for sites for which the two mates overlap the minimum of the average AS − XS for forward and reverse mates is taken). This filter is essential to remove mapping artefacts and a minimum AS − XS of 50 is applied also to the matched normal. (4) The average number of mismatches in a group of reads (forward or reverse) should not be higher than 2, either in the matched normal or the sample at hand. To avoid a bias in the filtering of mutation and reference calls, in cases in which a consensus base call is different from the reference, mismatches from that call are not considered when calculating the number of mismatches in the read. For sites at which the two mates overlap, the maximum of the average number of mismatches for forward and reverse mates is taken. (5) No 5′ clips are allowed. (6) No improper pairs are allowed in the read bundle to avoid unreliable mappings. (7) Base calls in read ends, defined as those within 8 bp from the 5′ or 3′ ends, are discarded because these regions are more likely to be unreliably mapped, especially when there are nearby indels. (8) Reads in the read bundle must contain no indels (except for indel calling). (9) The matched normal must have ≥15× coverage at a given site to make the risk of undetected heterozygous SNPs negligible. For non-neat matched normal samples, we also require that there are at least five reads aligned to each strand. (10) When a mutation is to be called, we require that the base is not seen with a frequency higher than 0.01 in the matched normal. (11) A site should not overlap the common SNP and noisy sites masks (see 'Genome masks'). Base calls that did not meet this requirement are also counted to obtain a qualitative diagnostic of potential contamination of the input DNA with DNA from a different individual.

Indel calling

To call indels we first identified read bundles with potential indels, defined as those containing sites with at least 90% of forward and reverse reads having an indel. Read bundles with AS − XS ≤ 50, 5′ clipping or with coverage in the matched normal lower than 16 were filtered out. Indels close to read ends (10 bp) were not called. For each of the read bundles that potentially contained an indel, the corresponding reads were extracted from the BAM file, removing PCR duplicate flags and creating a mini read bundle BAM. For each of the read bundle BAMs, we run samtools mpileup to generate genotype likelihoods in BCF format: samtools mpileup --no-BAQ -d 250 -m 2 -F 0.5 -r $chr:$start-$end −BCF --output-tags DP,DV,DP4,SP -f $ref_genome -o genotype_likelihods.bcf read_bundle.bam, where $chr, $start and $end are the mapping coordinates of the read bundle. Next, we call indels and normalize the output using the following three bcftools commands: (1) bcftools index -f genotype_likelihods.bcf genotype_likelihods.indexed.bcf; (2) bcftools call --skip-variants snps --multiallelic-caller --variants-only -O v genotype_likelihods.bcf -o bcftools.tmp.vcf; and (3) bcftools norm -f $ref_genome bcftools.tmp.vcf > bcftools.tmp2.vcf.

For each of the sites involved in an indel, we checked whether it overlapped a site masked by our common SNP and noise masks (see 'Genome masks'), in which case the indel is flagged as MASKED and not further analysed.

The final step involved revisiting the matched normal to inspect whether there are indels in a window of ±5 bp around each candidate indel. For this step we used the bam2R function from R package deepSNV[43]. Reads with mapping quality lower than 10 or with any of the following flags were ignored: 'read unmapped', 'not primary alignment', 'read fails platform/vendor quality checks', 'read is PCR or optical duplicate' and 'supplementary alignment'. If the proportion of indels in the matched normal within the ±5-bp window around the candidate somatic indel is higher than 1%, the indel is disregarded.

Substitution imbalances

To detect asymmetries in substitution patterns, variants were assigned to the forward or reverse strand according to their distance from fragmentation breakpoints. Variants closest to the 5′ of the forward read were assigned to the forward strand. Variants closest to the 5′ of the reverse read were assigned to the reverse strand and reverse complemented. Variants equidistant from both fragmentation breakpoints were not counted.

Genome masks

We applied two masks to filter duplex sequencing data. The first mask comprised common SNPs and spanned a total of 27,204,965 bp. Autosomal and X-chromosome common SNPs were defined as SNPs with allele frequency (AF) > 0.1% and a 'PASS' flag in gnomAD. Y-chromosome and mitochondrial SNPs were defined as SNPs with AF > 0.1% from the 1000 Genomes Project data[44,45]. This SNP mask is important to reduce the effect of potential inter-individual DNA contamination (Supplementary Note 6).

A second mask was developed to remove unreliable calls or sites prone to alignment artefacts. To build this noise mask, we gathered together gnomAD indel calls with AF > 1% and SNP calls with AF > 0.1%

that were not flagged as 'PASS'. The noise mask also contained sites with elevated error rates. To generate the mask, mismatch rates were calculated for every genomic position across a panel of 448 in-house standard whole-genome samples. Sites with mismatch rates (coverage-weighted mean variant allele frequency (VAF)) > 0.01 were incorporated into the noise mask. Altogether, the second mask comprised 22,474,160 bp.

Both masks are available as part of the supplementary code repository (https://zenodo.org/record/4604537).

Detection of human DNA contamination

Contamination of duplex sequencing libraries with DNA from other individuals could artificially inflate mutation burden estimates, mainly because germline SNPs in the contaminant DNA may appear as somatic mutations.

Even a small percentage of contamination can have a large effect on burden estimates. The burden associated with SNPs in the contaminant would be:

$$\text{Burden}_{\text{SNP}} = \frac{N_{\text{SNP}} f_{\text{cont}}}{G}$$

where N_{SNP} is the number of SNPs in the contaminant not shared with the sample at hand, f_{cont} the contamination fraction and G the size of the diploid human genome. Accordingly, 1% contamination would result in a $\text{Burden}_{\text{SNP}}$ of around 5×10^{-6} if there are 3 million non-shared SNPs. This burden is much higher than the somatic mutation rates that are usually observed.

First, we analysed how many SNPs across 2,504 individuals from the 1000 Genomes Project would remain after filtering with our common SNPs mask (n = 26,111,286; see 'Genome masks' section). Our results show that on average 55,685 SNPs would remain unfiltered for a given contaminant individual. Hence, for 1% contamination, filtering of common SNPs would reduce $\text{Burden}_{\text{SNP}}$ from 5×10^{-6} to 9×10^{-8} SNPs per bp. We note that the number of unfiltered SNPs varies largely across continental groups, with averages of 25,666 and 82,765 per individual in Europe and South Asia, respectively (Supplementary Note 6).

To estimate the extent of contamination we relied on VerifyBamID2[46], which we evaluated simulating contamination fractions below 1%, for both BAM files sequenced with standard methods and with the NanoSeq protocol (Extended Data Fig. 4e, f and Supplementary Note 6). To obtain more stable estimates we increased the number of markers from 100,000 to 500,000, by randomly choosing additional SNPs with minor allele frequency > 0.05 from the 1000 Genomes Project 20130502 release.

In silico decontamination

We detected that some libraries were contaminated with DNA from other analysed samples. In cases in which the contaminant could be identified, it is possible to remove the mutation calls corresponding to contaminant SNPs by using the corresponding BAM files. This simple approach proved useful to clean contaminated substitution calls and resulting mutation burden corrections were in line with VerifyBamId contamination estimates. That is, mutation burdens of non-contaminated samples remained unaltered after in silico decontamination, whereas the mutation burdens of contaminated samples decreased proportionally to the estimated contamination level.

This approach was applied to two plates for which some samples showed signs of contamination, including neurons, colonic crypts and smooth muscle samples. Mutation calls occurring at SNP sites in any of the other samples in the plate were removed. To accomplish this, we required that each mutation was supported by fewer than 10 base calls across the matched normal samples of potential contaminants and that the maximum support from any one matched normal was lower than 3 reads. All of the samples from plates showing evidence of contamination are considered as potential contaminants. Thresholds to remove contaminant calls were found empirically for the data at hand and should be adjusted when larger panels of matched normal samples or very high-coverage samples are analysed.

Indels were not analysed for nine samples with signs of contamination as we did not implement a decontamination pipeline for indels (Supplementary Table 4).

Correction of mutation burden and trinucleotide substitution profiles

Each library preparation method has its own fragmentation and amplification biases and captures a different subset of the total genome. For instance, amplification biases during library preparation often lead to lower coverage in GC-rich genomic regions[47]. As substitution rates show strong dependence on the trinucleotide context, taking into consideration differences in sequence composition can be important when comparing mutation burdens and substitution profiles between sequencing protocols. Biases can be particularly noticeable with NanoSeq restriction enzyme libraries, in which trinucleotides overlapping the restriction enzyme site (TGCA in the case of HpyCH4V) are depleted when read ends are filtered. There are 32 different trinucleotides in which the central nucleotide is a pyrimidine. Let t denote the count of a given trinucleotide of type $i = 1 \ldots 32$. The frequency of each trinucleotide is calculated separately for the genome f_i^g and for the NanoSeq experiment (weighted by the coverage at each site) f_i^e where:

$$f_i = \frac{t_i}{\sum_{i=1}^{32} t_i}$$

The ratio of genomic to experimental frequencies for a given trinucleotide is:

$$r_i = \frac{f_i^g}{f_i^e}$$

There are six classes of substitution for which the mutated base is a pyrimidine (C>A, C>G, C>T, T>A, T>C, T>G), and for each trinucleotide context there are three possible substitutions. Each trinucleotide–substitution count (for example, ATG>C, where T>C) is corrected by the ratio of genomic to experimental frequencies for the corresponding trinucleotide (ATG). For instance, let $s_{\text{ATG>C}}$ denote the count of substitution T>C in trinucleotide context ATG, the substitution count is corrected as follows:

$$s'_{\text{ATG>C}} = s_{\text{ATG>C}} r_{\text{ATG}}$$

This correction is applied to each of the 96 possible trinucleotide substitutions (h). The corrected substitution counts provide a substitution profile projected onto the human genome, and are also used to calculate the corrected mutation burden:

$$\beta' = \frac{\sum_{h=1}^{96} s'_i}{\sum_{i=1}^{32} t_i}.$$

Correction of NanoSeq mutation burden in cord blood by accounting for missed early embryonic mutations

Given their low burden, a substantial fraction of the mutation burden in cord blood HSC/MPP colonies is attributable to early embryonic mutations shared by multiple colonies. In the NanoSeq bioinformatics protocol, mutations with a VAF higher than 0.01 in the matched normal are considered germline SNPs and are filtered out from further analysis. Not accounting for the loss of early embryonic mutations can have a measurable effect on burden estimates in cord blood. Taking advantage of the availability of multiple HSC/MPP colonies per donor, we could quantify the loss of embryonic variants and correct the burden

estimate accordingly. For each of the 50 blood colonies we estimated the global VAF of each mutation in the remaining 49 colonies. This was done for the two neonatal donors. We determined that 24% of all the mutations called had a global VAF higher than 0.01. As a similar fraction of mutations would be missed by NanoSeq, we multiplied the NanoSeq estimated burden by a factor of 1.32, that is, 1/(1 − 0.24). A similar correction is not possible for the sperm burden estimates, as we lack single-cell level information for sperm, but a modest underestimation of the mutation burden due to missed embryonic variants is plausible.

Mutation calling in clonal samples sequenced with standard protocols

Mutation calls for HSPC colonies from donor PD43976_59yo were obtained from a previous study[26]. Mutation calls from standard whole-genome sequencing of colonic crypts[6] were obtained from a previous study[39]. Indel mutation calls for a bladder tumour sample (Extended Data Fig. 5) were obtained from a previously published study[34]. Indel calls for POLE and POLD1 mutants were obtained from a previous publication[48] (Extended Data Fig. 5).

For the HSC/MPP blood colonies sequenced in the present study, in-house pipelines were used to run CaVEMan and Pindel against an unmatched synthetic normal genome[49,50]. Another bespoke algorithm (cgpVAF) was then used to generate matrices of variant and normal reads at all sites that had a detected variant in any sample from a given individual. Up-to-date versions of these algorithms are available from the Sanger Institute's Cancer IT GitHub repository (https://github.com/cancerit).

Filtering strategies detailed below were then used to remove germline variants, technical artefacts and mutations that had arisen during culture in vitro. (1) A custom filter was used to remove artefacts associated with the 'low input' library preparation used, including those due to cruciform DNA structures. (2) A binomial filtering strategy was used to remove variants with aggregated count distributions consistent with germline SNPs. (3) A beta-binomial filter was used to remove low-frequency artefacts, that is, variants present at low frequencies across samples in a way that is not consistent with the sample-to-sample variation expected for acquired somatic mutations. (4) Sites with a mean depth below 8 and above 40 were removed. (5) Thresholds were used to filter out in vitro variants from the remaining mutations using a bespoke script. These were set to require a minimum variant read count of 2 or more and a variant allele fraction of 0.2 for autosomes and 0.4 for XY chromosomes. (6) The final filtering step involved building a phylogenetic tree from the HSC genomes derived from each individual. Mutations that did not fit the optimal tree structure were also discarded as likely artefacts.

Tree building was performed using MPBoot, which is a maximum-parsimony tree-approximation method[51]. Variants were genotyped as 'present' in a sample if two or more variant reads supported the variant. Variants were genotyped as 'absent' in a sample if zero variant reads were present at a given site and depth at that site was six or more. Sites that did not fall into either of the above categories were marked as 'unknown'. Mutations were assigned back to the tree using an R package (tree_mut), which uses a maximum-likelihood approach and the original count data to assign each mutation to a branch in the MPBoot generated tree.

Estimation of mutation burden in standard sequencing data

Using clonal or nearly clonal samples, we were able to compare NanoSeq to mutation burden estimates from standard whole-genome sequencing. This includes libraries prepared by laser microdissection and low-input enzymatic fragmentation[38] or sonication, followed by standard Illumina sequencing and mutation calling using CaVEMan[49]. The mutation calls described in the previous section were further processed to make burden estimates comparable across protocols.

To compare NanoSeq burdens to those from standard libraries, we restricted the analysis to regions of the genome covered by at least 20 reads in the standard libraries, to minimize the effect of low coverage on mutation calling sensitivity. We also excluded the fraction of the genome flagged as non-analysed by CaVEMan. Given the thorough filtering strategies applied for NanoSeq, we further restricted the analysed genome to include only sites callable in NanoSeq. Finally, given that trinucleotide frequencies in the callable genome of standard libraries differ from the background genomic frequencies, burden estimates were corrected accordingly. The difference in trinucleotide frequencies was mainly due to extensive filtering of common SNPs (frequent at CpG) and the partial depletion of trinucleotides overlapping the restriction site (TGCA). Remarkably, we found that estimates of mutation burden increased by around 20% in standard sequencing data when applying these corrections, largely due to reducing the effect of low sensitivity in certain genomic regions, either due to low coverage or mapping quality problems (Extended Data Fig. 5a, b and Supplementary Note 7).

Bootstrapped cosine similarity

Cosine similarities are frequently used to compare mutational profiles, although they do not consider the noise introduced by the number of mutations available. Small sample sizes can cause large cosine similarity deviations from their original spectrum. If a query profile (for example, NanoSeq result) with n mutations is compared to a reference profile, we can estimate the effect of small sample sizes by bootstrapping. From the reference profile, we obtained 1,000 random samples with size n, and calculated the cosine similarities of each of these samples to the reference profile, obtaining a 95% confidence interval. We can then calculate the cosine similarities between the query and the reference profiles and compare it to the 95% confidence interval from the bootstrapped samples.

Mutational signature analysis

Mutational signatures of single-base substitutions in their trinucleotide sequence context were inferred from sets of somatic mutation counts using the sigfit (v.2.0) package for R[52]. De novo signature extraction was performed for a range of numbers of signatures ($N = 2, \ldots, 8$), using counts of mutations grouped per tissue type (cord blood, adult blood, granulocytes, colonic crypts, smooth muscle or neurons) and sequencing method (NanoSeq or standard sequencing). To account for differences in sequence composition across samples, NanoSeq mutation counts were corrected as described in the 'Correction of mutation burden and trinucleotide substitution profiles' section. To avoid an excessive influence of tissue types more highly represented in our dataset, mutation counts were randomly downsampled to a maximum of 2,000 mutations from each tissue type. Samples with evidence of sporadic mutational processes, such as APOBEC or colibactin were removed from the dataset. This excluded urothelium, a bladder tumour sample and colonic crypts from one donor affected by colibactin (PD37449, $n = 3$). The best-supported number of signatures on the basis of overall goodness-of-fit, as reported by the 'extract_signatures' function in sigfit, was $N = 3$. The three extracted signatures (Fig. 3e) were subsequently fitted to the counts of mutations per sample (using the 'fit_signatures' function in sigfit) to infer the exposure of each signature in each sample.

Mutational signature analysis was also applied to publicly available single-cell mutation data from neurons[13]. Three signatures closely matching those shown in the original publication were extracted using the extract_signatures function in sigfit, with parameters nsignatures = 3, seed = 1469 and iter = 10000.

Linear regression modelling

Linear regressions were used to estimate the numbers of mutations accumulated per year, to test whether mutations associated with a given signature increased with age, or to test the effects of disease status or organ of origin on mutation burdens.

For neurons and urothelium, with only one sample per donor, we used simple multiple linear regressions (Supplementary Table 8), whereas

for the remaining cell types with multiple samples per donor (smooth muscle, colonic crypts, blood colonies, granulocytes and sperm) we used linear mixed-effect models, using donor as a random effect.

For simplicity, in the comparison of substitution and indel rates per year across all cell types shown in Fig. 3o, p, we used regression models without a free intercept, after verifying that the estimated intercepts were not significantly different from zero. All of the regression models, with and without intercepts, and their parameter estimates are summarized in Supplementary Table 8.

To test for the significance of a given fixed effect (such as organ of origin), we used the anova R function, comparing the null model without the fixed effect and the alternative model with the fixed effect (Supplementary Table 8). Confidence intervals for linear mixed-effects models at different ages were calculated using parametric bootstraping and 1,000 replicates, as implemented in the 'predict' method in the bootpredictlme4 R package.

All linear regression and statistical tests were conducted in R using packages: lm, lmer, afex, bootpredictlme4 and lmerTest.

Reporting summary

Further information on research design is available in the Nature Research Reporting Summary linked to this paper.

Data availability

Information on data availability for all samples is available in Supplementary Table 1. NanoSeq sequencing data have been deposited in the European Genome-phenome Archive (EGA; https://www.ebi.ac.uk/ega/) under accession number EGAD00001006459. Sperm samples are available from the EGA under accession number EGAD00001007028. Standard sequencing data have been deposited in the EGA under accession number EGAD00001006595. For publicly available samples, references to the original sources are provided in Supplementary Table 1. Substitution and indel rates are available in Supplementary Table 4. Substitution and indel calls for samples sequenced with NanoSeq are available in Supplementary Tables 5, 6. Trinucleotide substitution profiles are available in Supplementary Table 7. A detailed NanoSeq protocol is available in Protocol Exchange[53].

Code availability

The bioinformatics pipeline to process NanoSeq sequencing data comprises all steps including processing sequencing data, mapping, calling mutations and calculating corrected burden estimates and substitution profiles. This code is available from https://zenodo.org/record/4604537 (https://doi.org/10.5281/zenodo.4604537). Pipelines to call indels, perform signature extraction and signature fitting with sigfit, simulate the efficiency of the NanoSeq protocol, calculate the mutation burden in specific genomic regions and reproduce most of the main plots are also available from https://zenodo.org/record/4604537. Analyses in R were done with R v.3.3 and v.3.6. R libraries used include: GenomicRanges[54] (v.1.38.0), Rsamtools (v.2.2.3), MASS (v.7.3-51.5), sigfit[52] (v.2.0), readxl (v.1.3.1), deconstructSigs (v.1.8.0), lsa (v.0.73.2), deepSNV[55] (v.1.32.0), lme4 (v.1.1-26), afex (v.0.28-1), lmerTest (v.3.1-3), bootpredictlme4 (v.0.1) and Biostrings (v.2.54.0). Our pipeline makes use of samtools[56] v.1.9, bcftools[57] v.1.9, bwa v.0.7.5a-r405 and bedtools[58] v.2.29.0. We also used the following software: CaVeMan (v.2020), Pindel (v.2020) and MPBoot v.1.1.0.

38. Ellis, P. et al. Reliable detection of somatic mutations in solid tissues by laser-capture microdissection and low-input DNA sequencing. *Nat. Protocols* **16**, 841–871 (2021).
39. Olafsson, S. et al. Somatic evolution in non-neoplastic IBD-affected colon. *Cell* **182**, 672–684 (2020).
40. Krishnaswami, S. R. et al. Using single nuclei for RNA-seq to capture the transcriptome of postmortem neurons. *Nat. Protocols* **11**, 499–524 (2016).
41. Li, H. Aligning sequence reads, clone sequences and assembly contigs with BWA-MEM. Preprint at https://arxiv.org/abs/1303.3997 (2013).
42. Tischler, G. & Leonard, S. biobambam: tools for read pair collation based algorithms on BAM files. *Source Code Biol. Med.* **9**, 13 (2014).
43. Gerstung, M. et al. Reliable detection of subclonal single-nucleotide variants in tumour cell populations. *Nat. Commun.* **3**, 811 (2012).
44. Karczewski, K. J. et al. The mutational constraint spectrum quantified from variation in 141,456 humans. *Nature* **581**, 434–443 (2020).
45. The 1000 Genomes Project Consortium. A global reference for human genetic variation. *Nature* **526**, 68–74 (2015).
46. Zhang, F. et al. Ancestry-agnostic estimation of DNA sample contamination from sequence reads. *Genome Res.* **30**, 185–194 (2020).
47. Benjamini, Y. & Speed, T. P. Summarizing and correcting the GC content bias in high-throughput sequencing. *Nucleic Acids Res.* **40**, e72 (2012).
48. Robinson, P. S. et al. Elevated somatic mutation burdens in normal human cells due to defective DNA polymerases. Preprint at https://doi.org/10.1101/2020.06.23.167668 (2020).
49. Jones, D. et al. cgpCaVEManWrapper: simple execution of CaVEMan in order to detect somatic single nucleotide variants in NGS data. *Curr. Protoc. Bioinformatics* **56**, 15.10.1–15.10.18 (2016).
50. Raine, K. M. et al. Cgppindel: identifying somatically acquired insertion and deletion events from paired end sequencing. *Curr Protoc Bioinformatics* **52**, 15.17.1–15.17.12 (2015).
51. Hoang, D. T. et al. MPBoot: fast phylogenetic maximum parsimony tree inference and bootstrap approximation. *BMC Evol. Biol.* **18**, 11 (2018).
52. Gori, K. & Baez-Ortega, A. sigfit: flexible Bayesian inference of mutational signatures. Preprint at https://doi.org/10.1101/372896 (2020).
53. Lensing S. V. et al. Somatic mutation landscapes at single-molecule resolution. *Protocol Exchange* https://doi.org/10.21203/rs.3.pex-1298/v1 (2021).
54. Lawrence, M. et al. Software for computing and annotating genomic ranges. *PLOS Comput. Biol.* **9**, e1003118 (2013).
55. Gerstung, M., Papaemmanuil, E. & Campbell, P. J. Subclonal variant calling with multiple samples and prior knowledge. *Bioinformatics* **30**, 1198–1204 (2014).
56. Li, H. et al. The sequence alignment/map format and SAMtools. *Bioinformatics* **25**, 2078–2079 (2009).
57. Li, H. A statistical framework for SNP calling, mutation discovery, association mapping and population genetical parameter estimation from sequencing data. *Bioinformatics* **27**, 2987–2993 (2011).
58. Quinlan, A. R. & Hall, I. M. BEDTools: a flexible suite of utilities for comparing genomic features. *Bioinformatics* **26**, 841–842 (2010).
59. Kundaje, A. et al. Integrative analysis of 111 reference human epigenomes. *Nature* **518**, 317–330 (2015).

Acknowledgements We are grateful to the live donors and the families of the deceased organ transplant donors. We thank L. Anderson, K. Roberts, C. Latimer, Q. Lin, members of the CGP-lab, R. Vicario, F. Geissmann, N. Angelopoulos, G. Tischler, T. Bellerby, M. Abascal and K. Chatterjee for assistance in the development of NanoSeq or with this manuscript; all NIHR BioResource Centre Cambridge volunteers for participation; the NIHR BioResource Centre Cambridge and staff for their contribution; the National Institute for Health Research and NHS Blood and Transplant; the Cambridge Blood and Stem Cell Biobank for sample donation and support of this work; the Cambridge Brain Bank for sample donation; and the participants and local coordinators at the TwinsUK study. This research was supported by the Cambridge NIHR BRC Cell Phenotyping Hub. I.M. is funded by Cancer Research UK (C57387/A21777) and the Wellcome Trust. P.J.C. is a Wellcome Trust Senior Clinical Fellow. R.R. is a recipient of a CRUK Career Development fellowship (C66259/A27114). E.L. is supported by a Wellcome/Royal Society Sir Henry Dale Fellowship (grant number 107630/Z/15/Z), the European Hematology Association, BBSRC and by core funding from Wellcome (grant number 203151/Z/16/Z) and MRC to the Wellcome-MRC Cambridge Stem Cell Institute. D.G.K. is supported by a Bloodwise Bennett Fellowship (15008), the Bill and Melinda Gates Foundation (INV-002189) and an ERC Starting Grant (ERC-2016-STG–715371). The TwinsUK study was funded by the Wellcome Trust and European Community's Seventh Framework Programme (FP7/2007-2013). The TwinsUK study also receives support from the National Institute for Health Research (NIHR)-funded BioResource, Clinical Research Facility and Biomedical Research Centre based at Guy's and St Thomas' NHS Foundation Trust in partnership with King's College London. The views expressed are those of the author(s) and not necessarily those of the NHS, the NIHR or the Department of Health & Social Care.

Author contributions R.J.O., F.A. and I.M. conceived the project. I.M., P.J.C., R.R. and M.R.S. supervised the project. F.A., R.J.O., E.M. and I.M. wrote the manuscript; all authors reviewed and edited the manuscript. R.J.O. led the development of the protocol with help from F.A., A.R.J.L., P.E., S.V.L. and I.M. R.J.O. and F.A. developed the bioinformatics pipeline with help from R.E.A., S.L. and D.J. F.A. led the analysis of the data with help from A.R.J.L., I.M., A.B.-O., Y.W., L.M.R.H., E.J.K., T.H.H.C., M.S.C. and M.G. E.M. performed the HSC/MPP experiments. L.M.R.H. and A.J.C.R. performed the cell sorting of neuronal nuclei. A.R.J.L. and A.C. performed laser microdissection. E.M., N.F.Ø., H.E.M., M.D., D.G.K., E.L., K.T.M., K.S.-P., K.A., R.R., H.L.-S. and S.O. collected and processed samples. E.M., E.L., M.G. and D.G.K. assisted in the interpretation of blood data.

Competing interests A patent application on NanoSeq has been filed that includes R.J.O., F.A. and I.M.

Additional information

Supplementary information The online version contains supplementary material available at https://doi.org/10.1038/s41586-021-03477-4.

Correspondence and requests for materials should be addressed to R.J.O. or I.M.

Peer review information *Nature* thanks John Dick and the other, anonymous, reviewer(s) for their contribution to the peer review of this work. Peer reviewer reports are available.

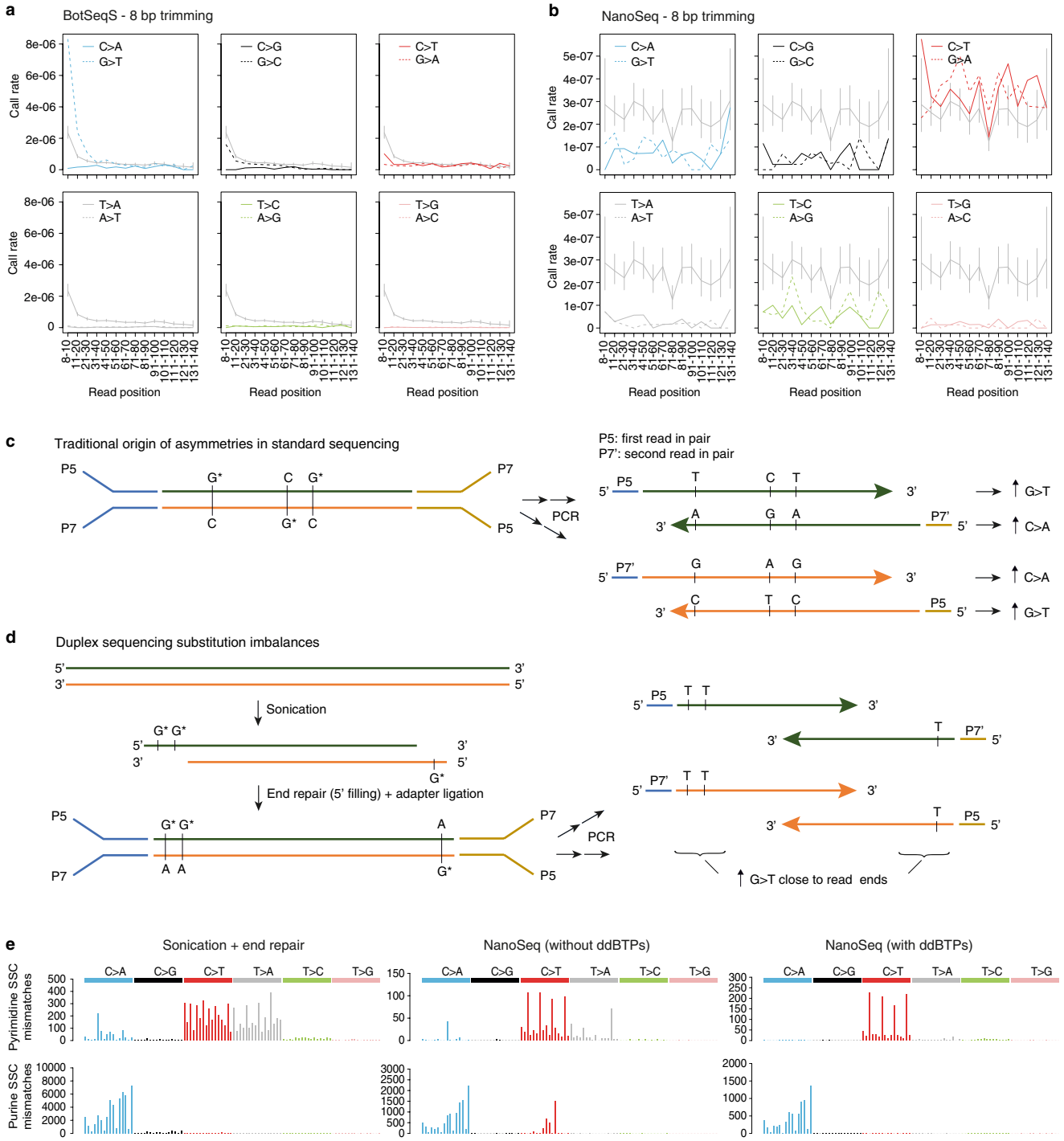

Extended Data Fig. 1 | Substitution imbalances and impact of A-tailing. **a**, **b**, Imbalances in the distribution of the six complementary substitutions (for example, G>T versus C>A) across read positions in BotSeqS (**a**) and NanoSeq (**b**). **c**, Origin of G>T over C>A mutation call imbalances in standard sequencing[22]. **d**, Origin of imbalances in duplex sequencing/BotSeqS as a result of end repair during library preparation. **e**, Single-strand consensus calls for pyrimidine (top) and purine (bottom) substitutions for the standard BotSeqS (left) protocol and for NanoSeq with standard (middle) and modified (right) A-tailing protocols. For example, C>T changes are shown at the top, whereas the complementary G>A changes are shown at the bottom. By using ddBTPs, C>A, G>A and T>A errors are reduced, lowering the risk of false-positive double-strand consensus calls.

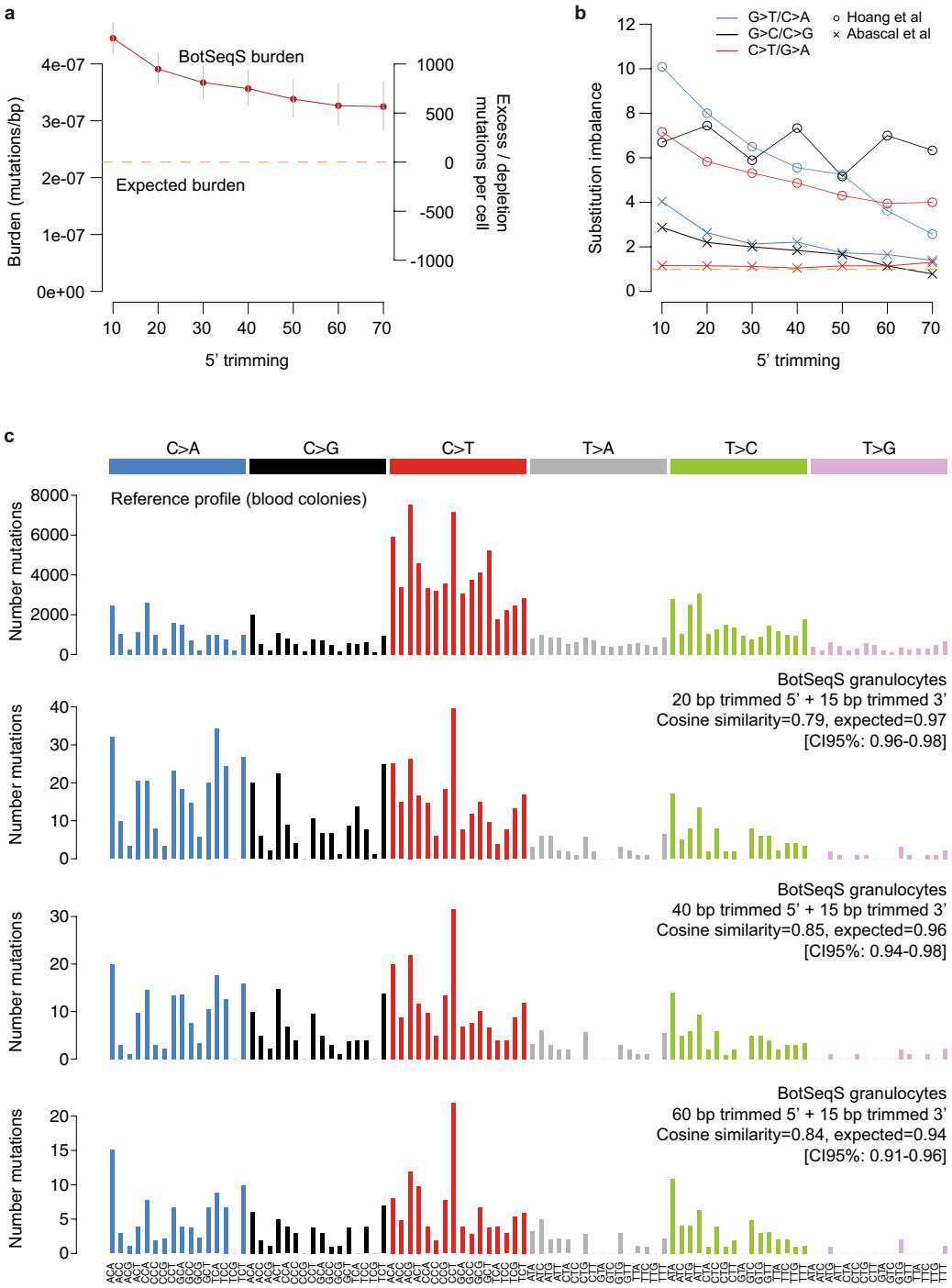

Extended Data Fig. 2 | BotSeqS errors as a function of read-end trimming. **a**, BotSeqS estimated burden for the granulocyte sample shown in Fig. 2c applying different extents of trimming to the 5′ ends of reads. Even with extensive trimming we predict at least 600 artifactual mutation calls per diploid genome. **b**, Substitution imbalances are observed deep into the reads and cannot be avoided with read trimming. Imbalances vary from experiment to experiment, as a consequence of DNA damage in the DNA source or during library preparation (Supplementary Note 1). **c**, Substitution profiles including the reference profile from single-cell-derived blood colonies and three BotSeqS profiles after trimming of 20, 40 and 60 bp from the 5′ end of reads (in addition to 15 bp trimming of the 3′ end). The text in the figure indicates the observed and expected cosine similarities (Methods) to the reference profile. C>A and C>G errors in BotSeqS remain after extensive trimming.

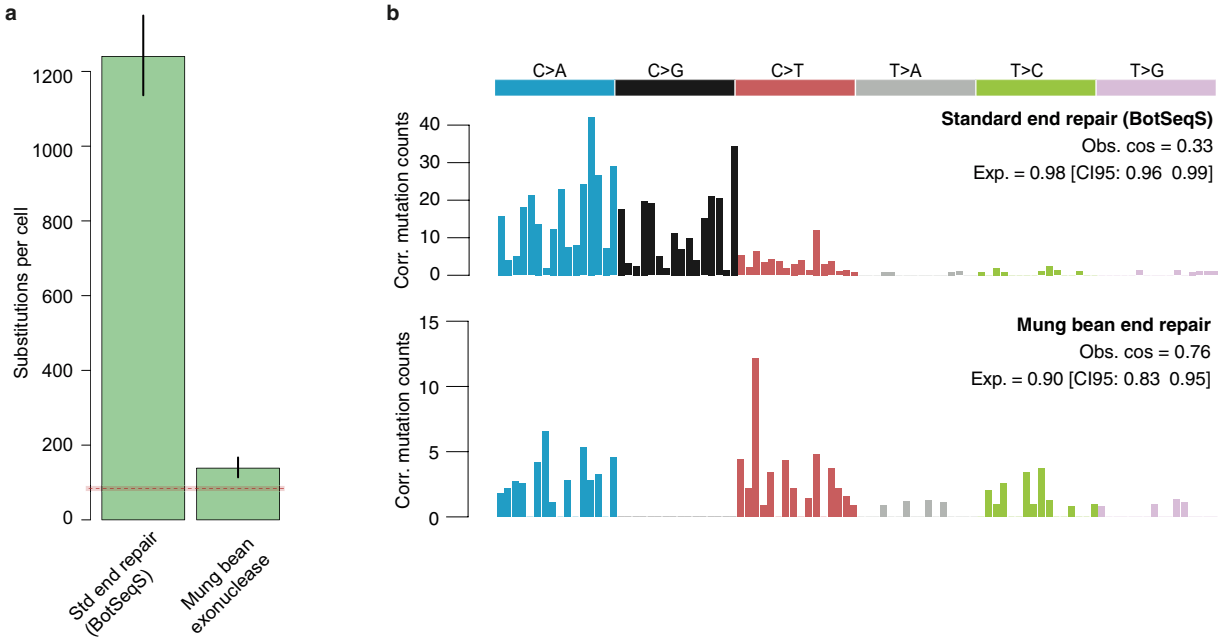

Extended Data Fig. 3 | Mung Bean NanoSeq. a, Estimated number of mutations per cord blood cell. Poisson 95% confidence intervals are shown as lines. The red dotted line shows the number of mutations per cord blood cell estimated with the restriction enzyme NanoSeq protocol, with Poisson 95% confidence intervals shown as a red shade. In contrast to Fig. 1f, we did not apply the correction for missing embryonic mutations because here we are comparing two protocols that are equally affected by this limitation. **b**, Substitution profiles for the standard end-repair protocol (BotSeqS) and for Mung Bean, showing the cosine similarities with the reference profile (Fig. 1c).

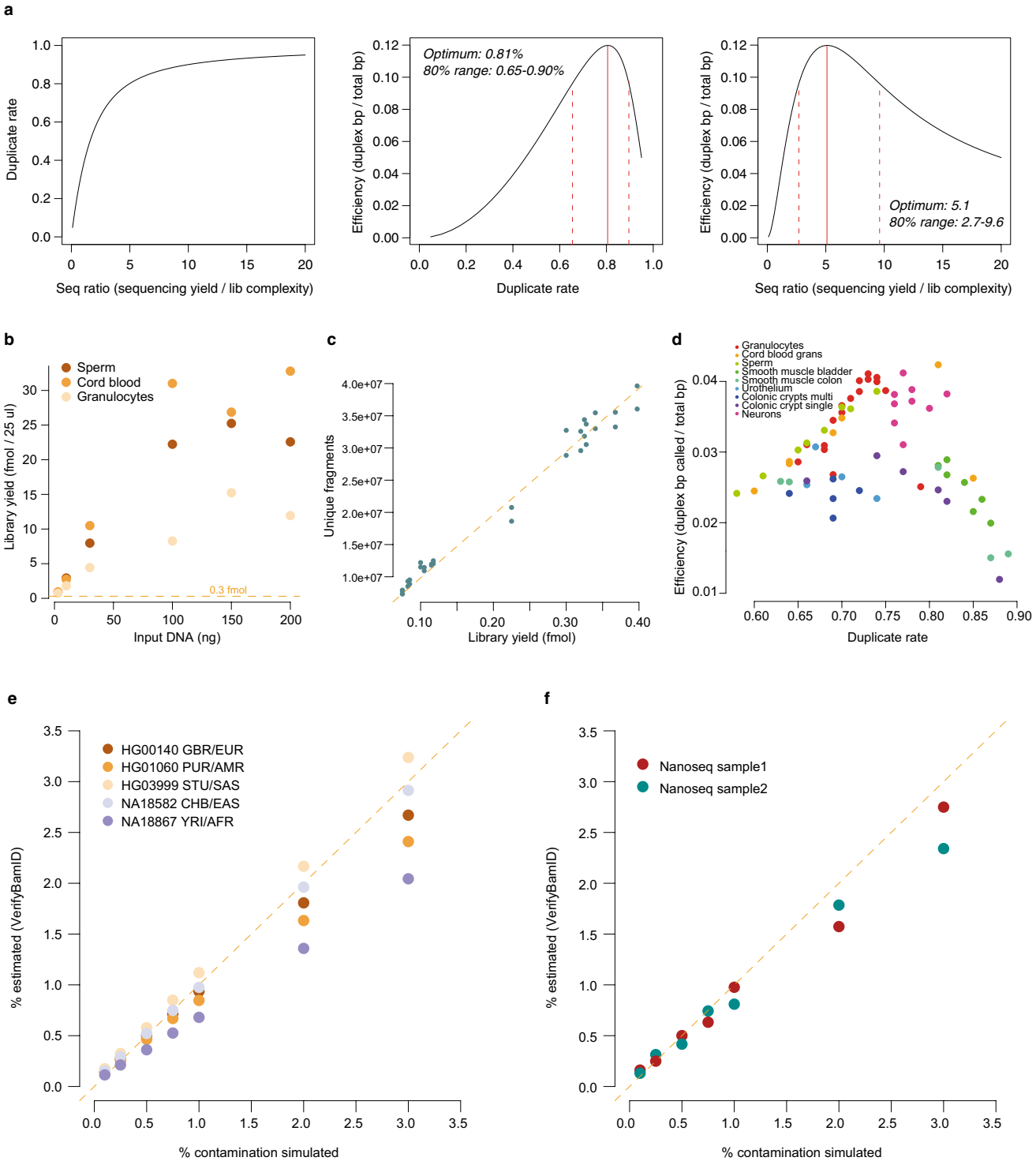

Extended Data Fig. 4 | Optimization of duplicate rates, DNA input requirements and estimation of human contamination. a, Relationship between sequencing yield, library complexity, duplicate rates and efficiency, based on a truncated Poisson model (Methods). Left, duplicate rate as a function of the sequencing ratio (sequencing reads/DNA fragments in the library). Middle, efficiency (measured as bases called with duplex coverage/bases sequenced) as a function of the duplicate rate. Right, efficiency as a function of sequencing ratio. **b**, Library yield as fmol per 25 µl as a function of the amount of input DNA in ng. **c**, Empirical relationship between the estimated fmol in library (measured by qPCR) and the number of unique molecules in the library estimated with Picard tools (Lander–Waterman equation) for our choice of restriction enzyme and fragment size selection (250–500 bp). **d**, Empirical relationship between duplicate rates and efficiency of the method, measured as duplex bases called/number of bases sequenced (that is, the number of paired-end reads multiplied by 300). The maximum efficiency (around 0.04) is lower than the maximum analytical expectation (0.12; middle panel in **a**) because of the trimming of read ends (barcodes, restriction sites and 8 bp from each end) and the strict filters that we apply to consider a site callable. **e**, VerifyBamId contamination estimates for different amounts of simulated contamination from individuals of different ancestry. **f**, Contamination simulation using two NanoSeq samples to contaminate each other.

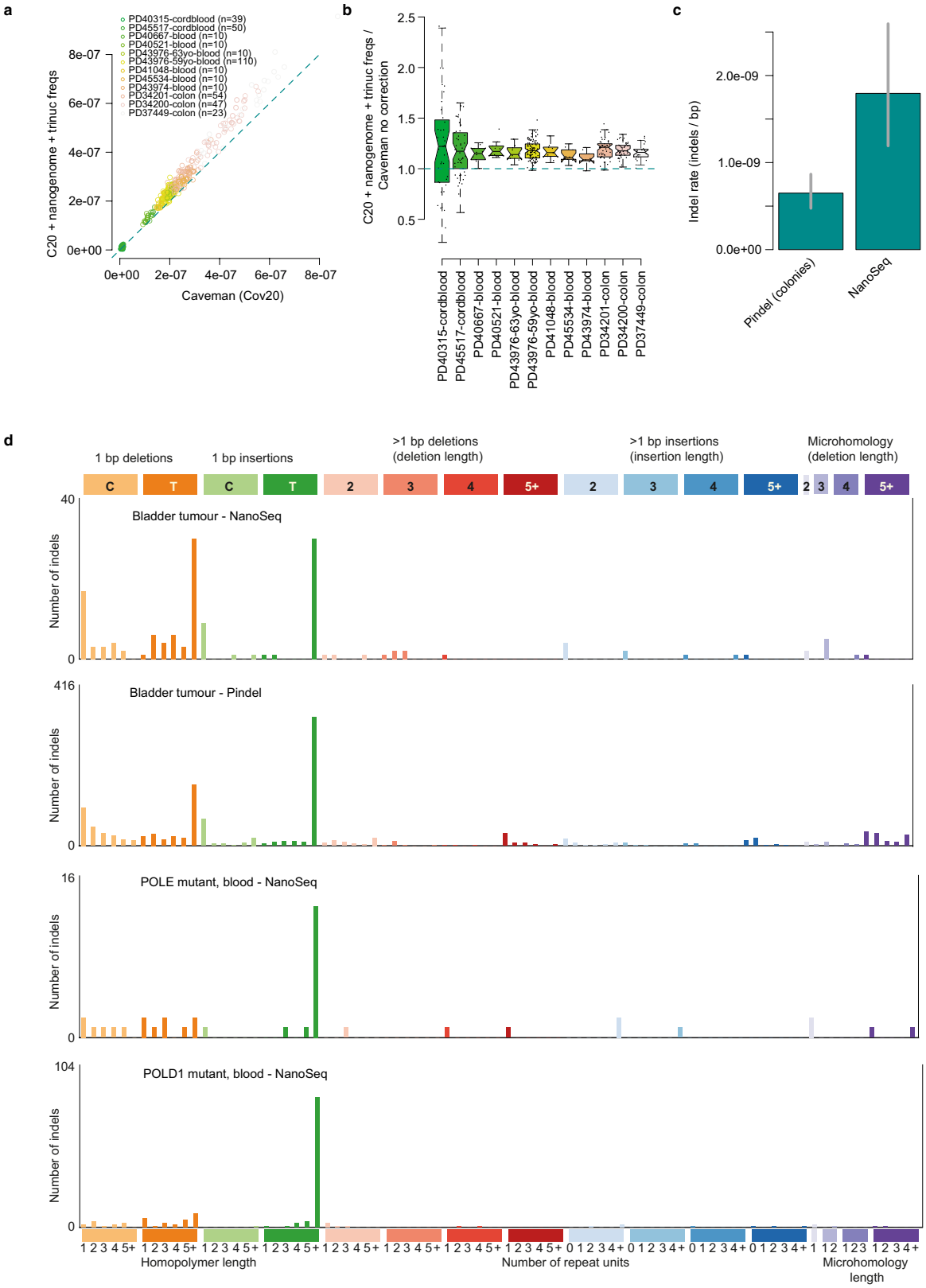

Extended Data Fig. 5 | Correction of standard (CaVEMan-based) mutation burden estimates and validation of NanoSeq indel calling. a, Comparison of the mutation burden estimates in regions of the genome with at least 20× coverage (*c*) to the trinucleotide-context-corrected mutation burdens in the subset of *c* covered by NanoSeq and passing all NanoSeq filters. **b**, Ratio between the rates shown in **a**, showing that the corrected burden is approximately 20% higher than the uncorrected burden; box plots show the interquartile range, median and 95% confidence interval for the median. **c**, Comparison of indel rates between cord blood colonies (indels were called with the Pindel algorithm) and granulocytes from neonates (NanoSeq pipeline), showing Poisson 95% confidence intervals. Given the sparsity of indel calls in cord blood, data from different colonies ($n = 100$) and granulocytes ($n = 2$ donors, one of them with 5 replicates) were combined into single point estimates. **d**, The top two panels show the high similarity between the NanoSeq and Pindel indel profiles for a bladder tumour; the bottom two profiles show the indel spectra in blood from *POLE* and *POLD1* germline mutation carriers, which are very similar to previously reported profiles[48].

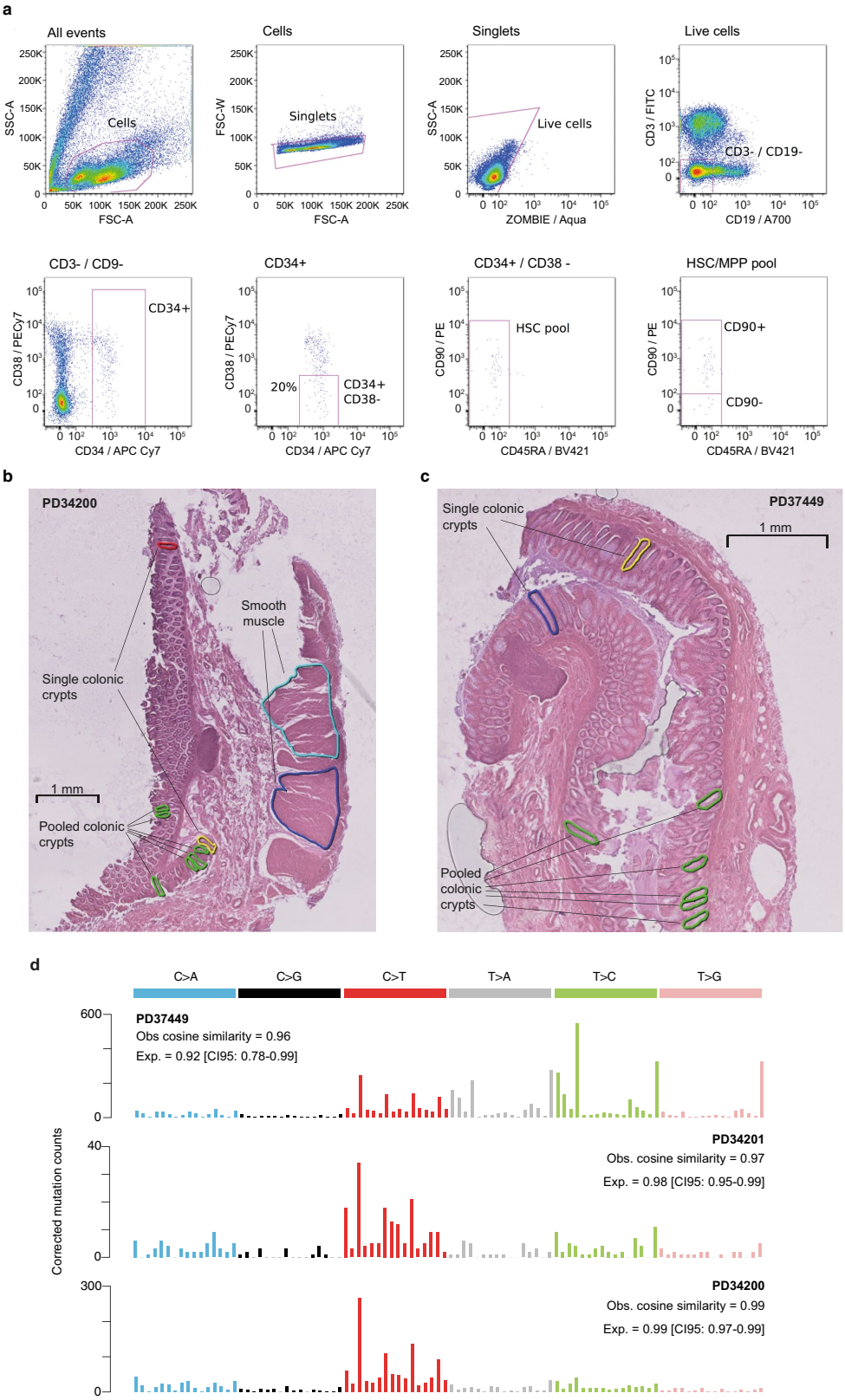

Extended Data Fig. 6 | Cell sorting of HSC/MPPs and colon histology. **a**, Gating strategy for the isolation of HSC/MPPs from a representative bone marrow sample. Text above the plots indicates the population depicted. Text inside the plots indicates the name of the gates shown in pink. The $CD34^+CD38^-$ population is defined as the bottom 20% $CD38^-$ as shown. For all initial samples (bone marrow, peripheral blood and cord blood), the index sorted population is the 'HSC pool' gate. Cell population abundance differed between samples but typically viable cells were 60–90% of total cells and singlets were 98–99% of viable cells. Live cells were 90–99% of viable cells and myeloid cells were 15–50% of live cells. $CD34^+$ cells were typically 1–15% of myeloid cells. **b**, **c**, Colon histology sections showing microbiopsied areas of colonic epithelium and smooth muscle for donors PD34200 (**b**) and PD37449 (**c**). For donor PD34200, a single crypt, a pool of six crypts and two smooth muscle areas were sequenced. For donor PD37449, the two single crypts and the pool of six crypts were sequenced. The burden estimates for these microbiopsies are shown in Figs. 2d, 3j, k. **d**, Substitution profiles for colonic crypts from the three donors in Fig. 2d and cosine similarities to profiles obtained with standard methods.

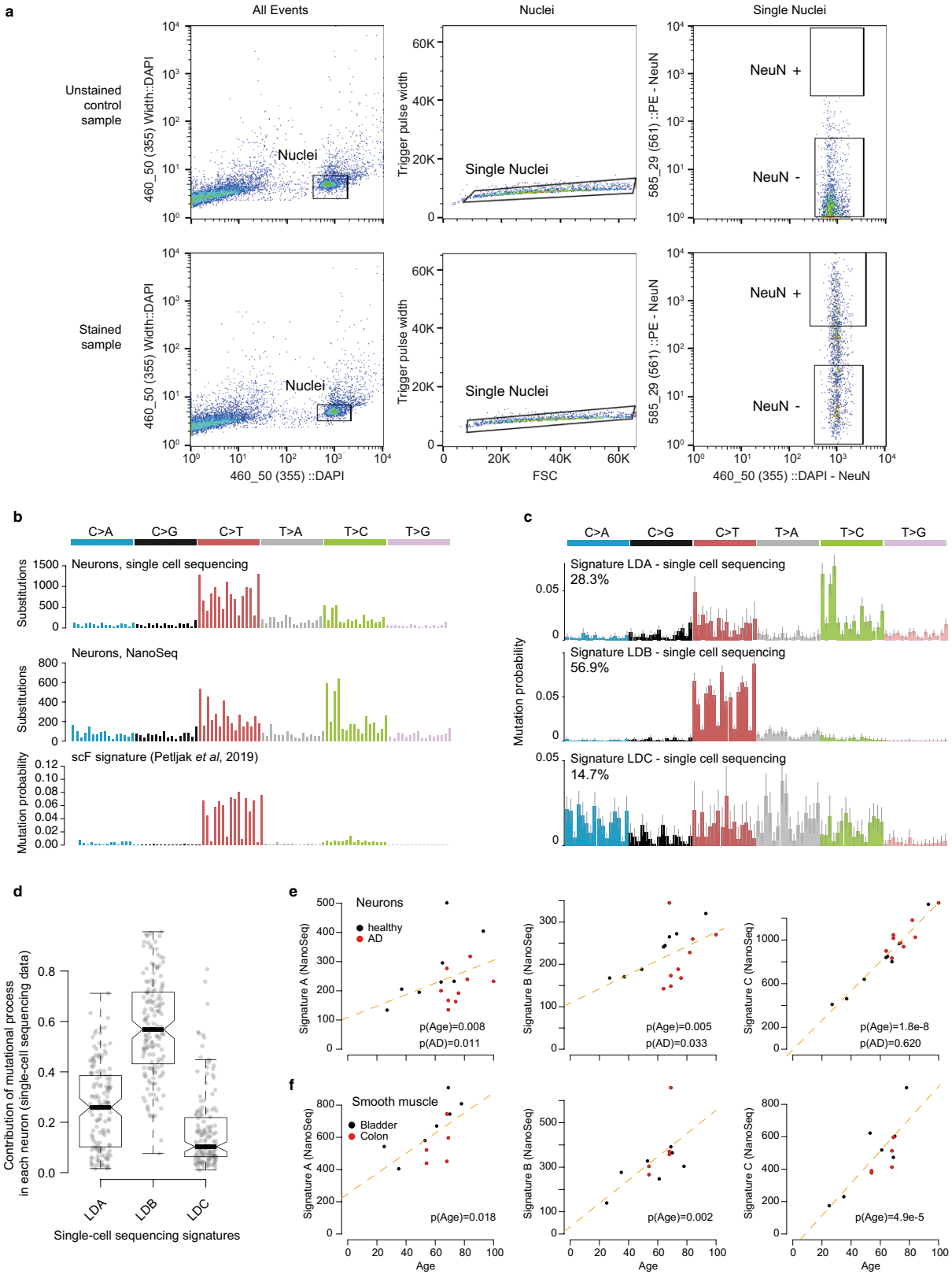

Extended Data Fig. 7 | See next page for caption.

Extended Data Fig. 7 | Neuron nuclei sorting, comparison to single-cell data and accumulation of mutations with age. a, Gating strategy for the isolation of neuronal nuclei from frontal cortex. Nuclei were sorted by FACS using an Influx cell sorter (BD Biosciences) with a 100-µm nozzle. For each sample an unstained control was used to help to determine the $NeuN^+$ population. The text above each column indicates the population depicted and the text inside the plots indicates the population of the gates highlighted in black. Sorting results varied among samples, with 1–60% passing the DAPI gate and, of these, 2–53% passing a conservative $NeuN^+$ gate. **b**, Substitution profiles for all mutations detected in neurons with SNP-phased error-corrected single-cell sequencing data from a previously published study[13] (top) and with NanoSeq (middle). Bottom, a signature specific to single-cell sequencing data is shown (scF signature from a previous publication[16]). **c**, Mutational signatures extracted from a previously published study[13], showing their relative contributions in the published dataset. These signatures were obtained using sigfit (Methods) on publicly available mutation calls and are referred to as LDA, LDB and LDC. Note the high similarity between the NanoSeq full spectrum for neurons and LDA (cosine similarity 0.96), and between scF and LDB (cosine similarity 0.97). **d**, Predicted contribution of LDA, LDB and LDC to each of the previously sequenced neurons[13]. **e**, Accumulation of mutations attributed to NanoSeq signatures A, B and C with age in healthy donors and in individuals with Alzheimer's disease. **f**, Accumulation of mutations attributed to NanoSeq signatures A, B and C in smooth muscle from bladder and colon.

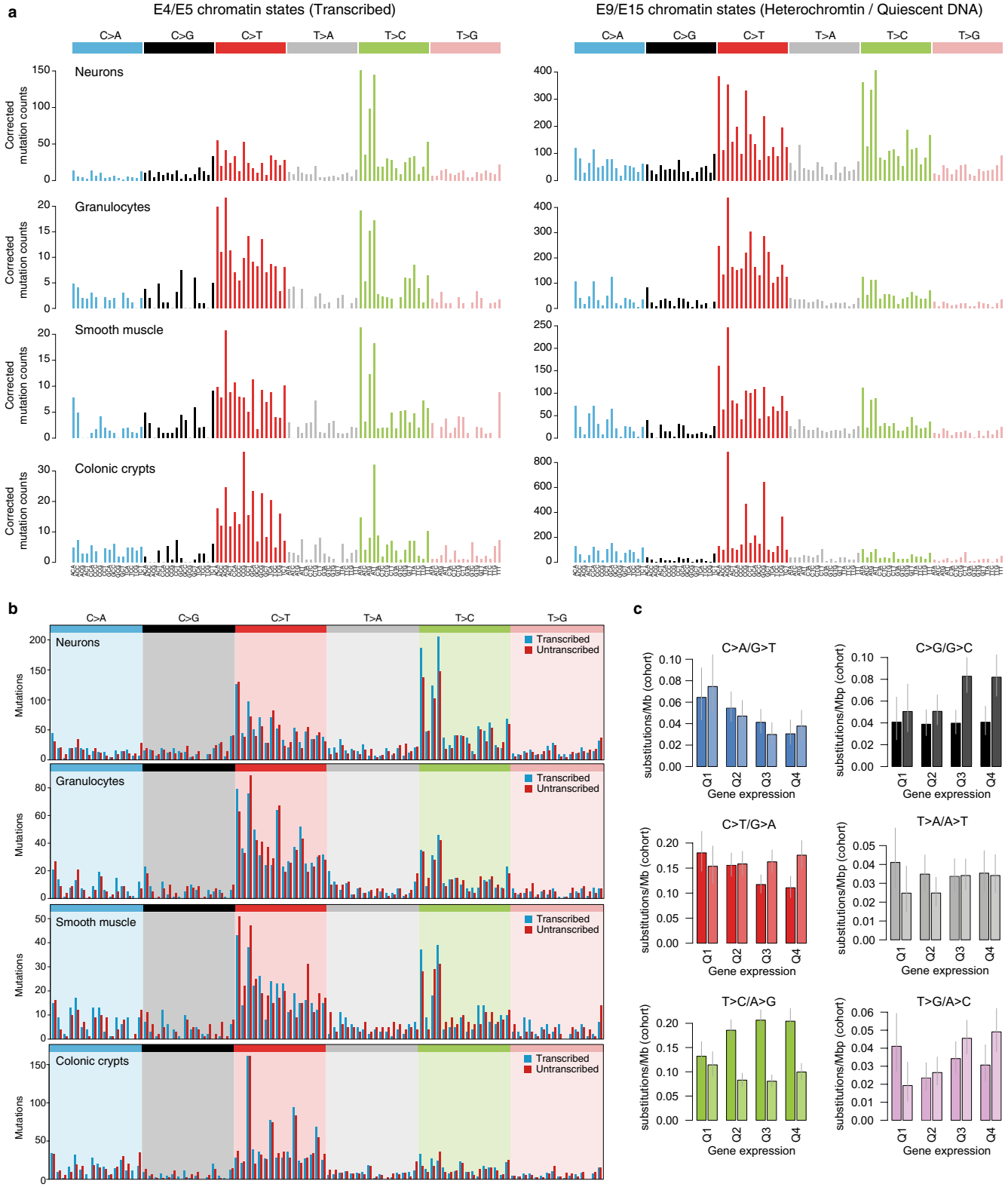

Extended Data Fig. 8 | Normalized substitution spectra across different genomic regions. a, Substitution spectra for neurons, granulocytes, smooth muscle and colonic crypts in chromatin states associated to transcription (states E4 and E5 in ENCODE) and inactive DNA (E9 and E15). Chromatin states were obtained from ENCODE[59], using the following epigenomes: E073 (frontal cortex), E030 (granulocytes), E076 (smooth muscle) and E075 (colonic mucosa). To enable the direct comparison of spectra across genomic regions with different trinucleotide frequencies, the profiles have been normalized to the genomic trinucleotide frequencies (Methods). **b**, Transcriptional strand asymmetries in neurons, granulocytes, smooth muscle and colonic crypts. **c**, Transcriptional strand asymmetries in neurons in quartiles of gene expression.

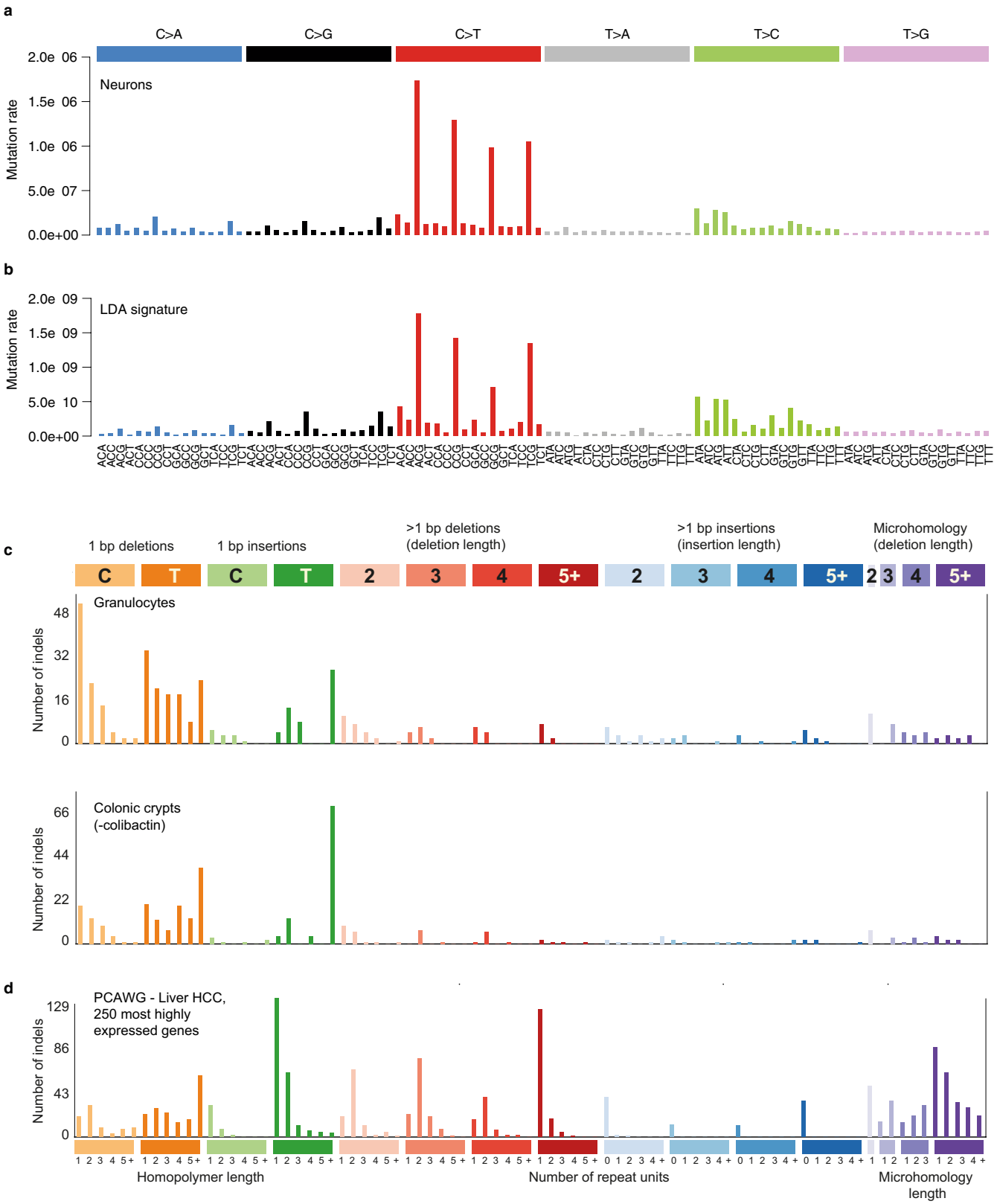

Extended Data Fig. 9 | Additional substitution and indel spectra. **a**, NanoSeq mutational spectrum for neurons corrected for trinucleotide frequency in the callable genome. Unlike the usual representation, which shows unnormalized rates, this representation shows mutation rates per available trinucleotide. **b**, Previously published LDA signature[13] normalized to trinucleotide frequency in the genome also reveals high C>T rates at CpG dinucleotides. This observation from single-cell data suggests that the high C>T rates at CpG sites in NanoSeq neuron data (**a**) are not caused by contamination of NeuN$^+$ pools with glia or other cells. **c**, Indel profiles of granulocytes (top) and colonic crypts without the colibactin signature (bottom). **d**, Indel profiles for the 250 most highly expressed genes in the PCAWG liver hepatocellular carcinoma data[31].

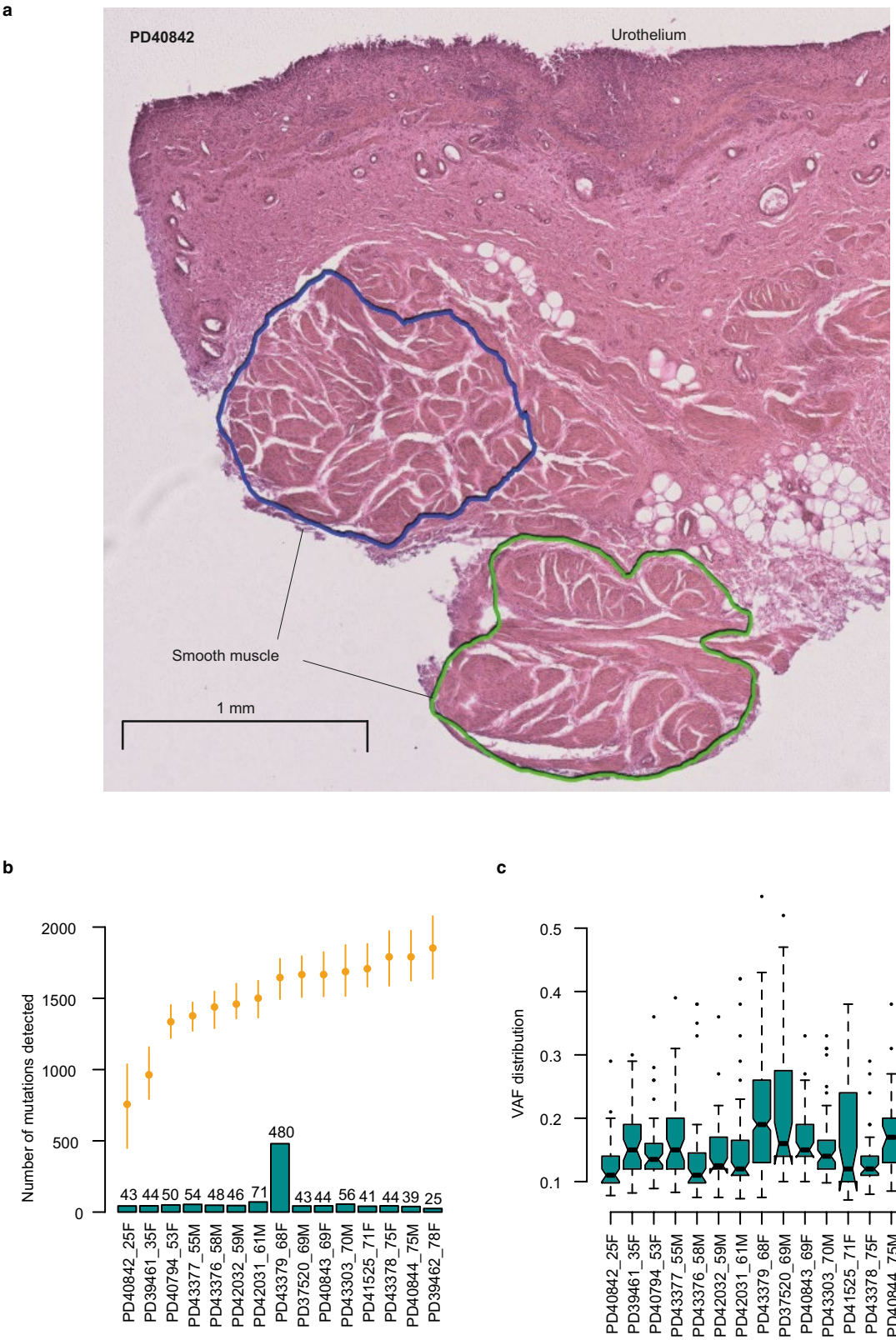

Extended Data Fig. 10 | Smooth muscle. a, Histology of bladder smooth muscle showing two sections from donor PD40842; only one of the two sections was sequenced using NanoSeq. **b**, Number of mutations detected with CaVEMan in different smooth muscle sections processed with our standard microdissection sequencing protocol[38]. The orange dots show the expected mutation burdens (with 95% confidence intervals) for these sections based on the donor age and the regression model shown in Fig. 3j. **c**, Distribution of VAFs for each of the smooth muscle sections using standard whole-genome sequencing. Box plots show the interquartile range, median, 95% confidence interval for the median (notches), and outliers (black dots).

nature research

Corresponding author(s): Robert J. Osborne, Iñigo Martincorena

Last updated by author(s): Mar 12, 2021

Reporting Summary

Nature Research wishes to improve the reproducibility of the work that we publish. This form provides structure for consistency and transparency in reporting. For further information on Nature Research policies, see our Editorial Policies and the Editorial Policy Checklist.

Statistics

For all statistical analyses, confirm that the following items are present in the figure legend, table legend, main text, or Methods section.

n/a	Confirmed	
☐	☒	The exact sample size (*n*) for each experimental group/condition, given as a discrete number and unit of measurement
☐	☒	A statement on whether measurements were taken from distinct samples or whether the same sample was measured repeatedly
☒	☐	The statistical test(s) used AND whether they are one- or two-sided *Only common tests should be described solely by name; describe more complex techniques in the Methods section.*
☐	☒	A description of all covariates tested
☐	☒	A description of any assumptions or corrections, such as tests of normality and adjustment for multiple comparisons
☐	☒	A full description of the statistical parameters including central tendency (e.g. means) or other basic estimates (e.g. regression coefficient) AND variation (e.g. standard deviation) or associated estimates of uncertainty (e.g. confidence intervals)
☒	☐	For null hypothesis testing, the test statistic (e.g. *F*, *t*, *r*) with confidence intervals, effect sizes, degrees of freedom and *P* value noted *Give P values as exact values whenever suitable.*
☒	☐	For Bayesian analysis, information on the choice of priors and Markov chain Monte Carlo settings
☐	☒	For hierarchical and complex designs, identification of the appropriate level for tests and full reporting of outcomes
☐	☒	Estimates of effect sizes (e.g. Cohen's *d*, Pearson's *r*), indicating how they were calculated

Our web collection on statistics for biologists contains articles on many of the points above.

Software and code

Policy information about availability of computer code

Data collection	No software was used for data collection.
Data analysis	Most analyses have been done with bespoke pipelines, deposited in https://github.com/fa8sanger/NanoSeq_Paper_Code and https://github.com/cancerit. Analyses in R were done with R v3.3 and v3.6. R libraries used include: GenomicRanges (v1.38.0), Rsamtools (v2.2.3), MASS (v7.3-51.5), sigfit (v2.0), readxl (v1.3.1), deconstructSigs (v1.8.0), lsa (v0.73.2), deepSNV (v1.32.0), lme4 (v1.1-26), afex (v0.28-1), lmerTest (v3.1-3), bootpredictlme4 (v0.1), Biostrings (v2.54.0). Our pipeline makes use of samtools v1.9, bcftools v1.9, bwa v0.7.5a-r405, bedtools v2.29.0. We also used the following programs: CaVeMan (v 2020), Pindel (v 2020), MPBoot 1.1.0.

For manuscripts utilizing custom algorithms or software that are central to the research but not yet described in published literature, software must be made available to editors and reviewers. We strongly encourage code deposition in a community repository (e.g. GitHub). See the Nature Research guidelines for submitting code & software for further information.

Data

Policy information about availability of data

All manuscripts must include a data availability statement. This statement should provide the following information, where applicable:

- Accession codes, unique identifiers, or web links for publicly available datasets
- A list of figures that have associated raw data
- A description of any restrictions on data availability

Information on data availability for all samples is included in Supplementary Table 1. NanoSeq sequencing data has been deposited in EGA under accession number EGAD00001006459. Standard sequencing data has been deposited in EGA under accession number EGAD00001006595. For samples publicly available, references to the original sources are provided in Supplementary Table 1. Substitution and indel calls for samples sequenced with NanoSeq are available in Supplementary Table 1.

Field-specific reporting

Please select the one below that is the best fit for your research. If you are not sure, read the appropriate sections before making your selection.

☒ Life sciences ☐ Behavioural & social sciences ☐ Ecological, evolutionary & environmental sciences

For a reference copy of the document with all sections, see nature.com/documents/nr-reporting-summary-flat.pdf

Life sciences study design

All studies must disclose on these points even when the disclosure is negative.

Sample size	Information on sample sizes is provided for all analyses. We estimated that, with optical duplicate rates, sequencing coverage translates into effective coverage on a 1/20 ratio. The requested sequencing coverage was chosen to obtain approximately 3 Gb of duplex coverage for each sample. We estimated analytically and empirically that to obtain 3 Gb of duplex coverage about 20*3 Gb of raw sequencing data are needed (about 2e8 read pairs). 3 Gb of coverage provide about 700 mutations in a typical somatic tissue in a middle age individual. This number of mutations is well suited for mutation burden estimates, signature analysis, and comparisons across donors. Given their very low mutation burdens, for cord blood and sperm more data was requested by sequencing multiple replicates from each individual (n=7 for one of the sperm donors; n=6 for the cord blood donor). Sequencing yields, duplicate rates and effective duplex coverages are available in Supplementary Table 1. Samples were selected based on availability, maximising age span across donors and representation from both genders. Ages and gender are available in Supplementary Table 1.
Data exclusions	The distributions of NeuN-PE intensities in most samples revealed a bimodal distribution. As a quality control, we fitted a mixture of two Gamma distributions to the NeuN-PE intensities for every samples. Only samples with 10-fold (1 log10 unit) separation between the mean of both peaks were considered for analysis, which led to the exclusion of an outlier sample. The exclusion criteria was applied a posteriori after realising the outlier sample had bad sorting quality metrics.
Replication	Different replicates were run for granulocytes (59 y.o. donor, n=6), cord blood (n=6), sperm (n=7), colonic crypts (n=2 for two donors), and smooth muscle (n=2 for two donors). Variation in mutation burden estimates across replicates was in all cases compatible with expected Poisson variation.
Randomization	No randomization was performed.
Blinding	No blinding was undertaken.

Reporting for specific materials, systems and methods

We require information from authors about some types of materials, experimental systems and methods used in many studies. Here, indicate whether each material, system or method listed is relevant to your study. If you are not sure if a list item applies to your research, read the appropriate section before selecting a response.

Materials & experimental systems

n/a	Involved in the study
☐	☒ Antibodies
☒	☐ Eukaryotic cell lines
☒	☐ Palaeontology and archaeology
☒	☐ Animals and other organisms
☐	☒ Human research participants
☒	☐ Clinical data
☒	☐ Dual use research of concern

Methods

n/a	Involved in the study
☒	☐ ChIP-seq
☐	☒ Flow cytometry
☒	☐ MRI-based neuroimaging

Antibodies

Antibodies used	Milli-Mark Anti-NeuN-PE, clone A60 (1:500; Supplier number: MilliPore, FCMAB317PE; Lot Numbers: 3153277, 3227873). CD3 (1:500; BD, Catalog Number: 555339, Clone: HIT3a); CD90 (1:50; Biolgend, Catalog Number: 328110, Clone: 5E10); CD49f (1:100; BD, Catalog Number: 551129, Clone: GoH3); CD19 (1:300; Biolgend, Catalog Number: 302226, Clone: HIB19); CD34 (1:100; Biolgend, Catalog Number: 343514, Clone: 581); Zombie (1:2000; Biolgend, Catalog Number: 423101, Clone: NA); CD38 (Biolgend, Catalog Number: 303516, Clone: HIT2); CD45RA (1:100; Biolgend, Catalog Number: 304130, Clone: HI100)
Validation	NeuN-PE validation: https://www.citeab.com/antibodies/225077-fcmab317pe-milli-mark-anti-neun-pe-antibody-clone-a6. We have also validated the specificity of this antibodies with non-neuronal samples. Blood Ab validations available at BD and Biolgend manufacterers. References: CD3 (Beverley PC et al. Eur J Immunol. 1981; 11(4):329-334.); CD90 (Adutler-Lieber S, et al. 2013. J Cardiovasc Pharmacol Therap. 18:78.); CD49f (Aumailley et al. Exp Cell Res. 1990; 188(1):55-60.); CD19 (Boyle M, et al. 2015. J Infect

Dis. 212: 416-425.); CD34 (Bigley V, et al. 2011. J Exp Med. 208:227.); Zombie (Berg J, et al. 2013. J Exp Med. 210:2803.); CD38 (Chaimowitz N, et al. 2011. J Immunol. 187:5114.); CD45RA (Causi E, et al. 2015. PLoS One. 10: 0136717.)

Human research participants

Policy information about studies involving human research participants

Population characteristics	Brain samples of healthy and Alzheimer's disease donors were requested to the Cambridge Brain Bank. The 8 samples from healthy donors spanned ages 27-93 (average of 59.5), with four males and four females. The 9 Alzheimer's disease donors spanned ages 64-84 (73.3) and included 2 males and 7 females (Supplementary table 1). No treatment information was compiled. Blood samples were obtained from healthy donors, with a balance gender representation (9 males, 7 females) and spanning a wide range of ages (20-81; average of 56.1). Cord blood samples were obtained from three females and one male. These samples were obtained from: StemCell Technologies, Cambridge Blood and Stem Cell Biobank, Cambridge Biorepository for Translational Medicine, and Cambridge Bioresource. Smooth muscle (25-78 years old; average of 58.2; 3 males, 7 females), bladder (25-78 years old; average of 56.2; 4 females) and colon samples (36-68 years old; average of 53; 3 males, 2 females) were obtained from deceased organ donors with the consent of families. No treatment information was compiled.
Recruitment	Samples were chosen based on availability at the Cambridge Brain Bank, the Cambridge Blood and Stem Cell Biobank, the Cambridge Biorepository for Translational Medicine, and the Cambridge Bioresource. We attempted to obtain a balanced gender representation and a wide range of ages whenever possible. For brain samples, a balance between healthy and Alzheimer's disease donors was also requested.
Ethics oversight	Informed consent was obtained from all donors or their families. The study complies with all relevant ethical regulations. REC references: 07-MRE05-44, 18/EE/0199, 15/EE/0152 - NRES Committee East of England - Cambridge South; EC04/015, London - Westminster REC; 16/NE/003, NRES Committee North East-Newcastle and North Tyneside 1; 15/EE/0152 NRES Committee East of England – Cambridge South; 10/H0308/56, East of England, Nottingham

Note that full information on the approval of the study protocol must also be provided in the manuscript.

Flow Cytometry

Plots

Confirm that:

☒ The axis labels state the marker and fluorochrome used (e.g. CD4-FITC).

☒ The axis scales are clearly visible. Include numbers along axes only for bottom left plot of group (a 'group' is an analysis of identical markers).

☒ All plots are contour plots with outliers or pseudocolor plots.

☒ A numerical value for number of cells or percentage (with statistics) is provided.

Methodology

Sample preparation	Neuronal nuclei were isolated, stained and extracted from the frontal cortex samples as per Krishnaswami et al.39. Briefly, small cuts of 1-2 mm were taken from fresh frozen samples. Dounce homogenisation was then used to free nuclei before filtration, density centrifugation and immunostaining. Samples were stained using DAPI (Thermo Fisher, D1306) and Milli-Mark™ Anti-NeuN-PE Antibody (MilliPore, FCMAB317PE). Blood samples preparation is described in the relevant methods section.
Instrument	Neuron nuclei were sorted by FACS using an Influx Cell Sorter (BD Biosciences, Model Number 646500P7 – INFLUX 2B3R6V4UV5YG BSC Serial/Lot Number:X646500P7001) with a 100-µm nozzle. The Influx Cell Sorter software used was BD FACS Sortware 1.2.0.142. Blood cells were sorted using Aria Fusion and BD Aria III instruments.
Software	Neuron nuclei: FlowJo 10.6.1 (Operating System: Mac OS X Java Version: 1.8.0_151-b12). Blood cells: BD Diva and FlowJo v9.6
Cell population abundance	Neuron nuclei: Sorting results varied among samples, with 1-60% passing the DAPI gate and, of these, 2-53% passing a conservative NeuN+ gate; percentages of nuclei passing gates are summarised in Extended Data Figure 7 legend Blood cells: Cell population abundance differed between samples but typically viable cells were 60-90% of total cells and singlets were 98-99% of viable cells. Live cells were 90-99% of viable cells and myeloid cells were 15-50% of live cells. CD34+ cells were typically 1-15% of myeloid cells; included in Extended Data Figure 6 legend.

Gating strategy

Neuron nuclei: flow sorted samples were passed through three gates, DAPI vs DAPI width to identify DNA staining nuclei, Trigger pulse width vs FSC to identify singlets, NeuN-PE vs DAPI to identify neuronal nuclei (Methods and Extended Data Figure 7).
Blood cells: the details are provided in the relevant methods section and in Extended Data Figure 6.

☒ Tick this box to confirm that a figure exemplifying the gating strategy is provided in the Supplementary Information.